Tropospheric ozone column dataset from OMPS-LP/OMPS-NM limb-nadir matching

Andrea Orfanoz-Cheuquelaf[1], Carlo Arosio[1], Alexei Rozanov[1], Mark Weber[1],
Annette Ladstätter-Weißenmayer[1], John P. Burrows[1], Anne M. Thompson[2,3], Ryan M. Stauffer[2], and
Debra E. Kollonige[2,4]

[1]Institute of Environmental Physics, University of Bremen, Otto-Hahn-Allee 1, D-28359 Bremen, Germany
[2]Earth Sciences Division, NASA/Goddard Space Flight Center, Greenbelt, MD, USA
[3]GESTAR and Joint Center for Earth Systems Technology, University of Maryland, Baltimore County, Baltimore, MD, USA
[4]Science Systems and Applications, Inc., Lanham, MD, USA

Correspondence: Andrea Orfanoz-Cheuquelaf (andrea@iup.physik.uni-bremen.de)

Abstract.

A Tropospheric Ozone Column (TrOC) dataset from the Ozone Mapping and Profiler Suite (OMPS) observations was generated by combining the retrieved total ozone column from OMPS - Nadir Mapper (OMPS-NM) and limb profiles from OMPS - Limb Profiler (OMPS-LP) data. All datasets were generated at the University of Bremen, and the TrOC product was obtained by applying the Limb-Nadir Matching technique (LNM). The retrieval algorithm and a comprehensive analysis of the uncertainty budget are presented here. The OMPS-LNM-TrOC dataset (2012-2018) is analysed and validated by comparing with ozonesondes, tropospheric ozone residual (TOR) data from the combined Ozone Monitoring Instrument/Microwave Limb Sounder (OMI/MLS) observations, and the TROPOspheric Monitoring Instrument (TROPOMI) Convective Cloud Differential technique (CCD) dataset. The OMPS-LNM TrOC is generally lower than the other datasets. The average bias with respect to ozonesondes is -1.7 DU with no significant latitudinal dependence identified. The mean difference with respect to OMI/MLS TOR and TROPOMI CCD is -3.4 and -1.8 DU, respectively. The seasonality and inter-annual variability are in good agreement with all comparison datasets.

1 Introduction

Ozone (O_3) in the troposphere is a harmful pollutant and a ~~near-term climate forcer (Shindell et al., 2006; Stevenson et al., 2013; Schultz et~~ short-lived climate forcer (Shindell et al., 2006; Stevenson et al., 2013; Schultz et al., 2015; Szopa et al., 2023). There are two sources of tropospheric O_3: photochemical production and transport from the stratosphere. Sources of chemical precursors of this secondary pollutant originate from biomass burning, lightning and anthropogenic emissions. Tropospheric O_3 concentration depends on local production and losses, as well as long-range transport (Archibald et al., 2020). Additional contributions come from intrusions of stratospheric O_3 (e.g. Škerlak et al., 2014). The ~~residence time of in the continental boundary layer is in the range of a few days, while in the free troposphere, the annual mean lifetime of~~ global average lifetime of tropospheric O_3 ~~is around 40 days (Kourtidis, 2002).~~ was estimated to be 22-23 days (Young et al., 2013).

A global assessment of the amount and evolution of tropospheric O_3 is potentially possible by using passive remote sensing by space-borne instruments (e.g. Gaudel et al., 2018; Heue et al., 2016; Leventidou et al., 2018). The retrieval of tropospheric O_3 from the measurements of satellite sensors started in the late 1980s. One of the commonly used methods is the integration over the troposphere of the O_3 profiles retrieved from nadir measurements in the infrared (IR) or ultraviolet (UV) spectral range. Tropospheric O_3 from nadir profiles is available, for example, from the Infrared Atmospheric Sounding Interferometer (IASI), Greenhouse gases Observing SATellite (GOSAT), Global Ozone Monitoring Experiment 2 (GOME-2), and TROPOspheric Monitoring Instrument (TROPOMI) (Boynard et al., 2009; Ohyama et al., 2012; Miles et al., 2015; Mettig et al., 2022). The disadvantage of this approach is that the profiles may be less sensitive to changes in boundary layer O_3 (Doche et al., 2014). The accuracy of this technique is limited by a relatively coarse vertical resolution (7-10 km) of the retrieved profiles (see e.g. Mettig et al., 2022, and references therein).

Another method to obtain tropospheric O_3 columns (TrOC) from nadir-viewing satellite measurements is the Convective Cloud Differential technique (CCD). This technique has been applied to the series of Total Ozone Mapping Spectrometers (TOMS) and Global Ozone Monitoring Experiment (GOME) instruments, the SCanning Imaging Absorption spectroMeter for Atmospheric CHartographY (SCIAMACHY) and TROPOMI (Ziemke et al., 1998; Valks et al., 2014; Leventidou et al., 2016; Ziemke et al., 2019; Hubert et al., 2021; Heue et al., 2021). In simple terms, this method subtracts the O_3 column retrieved above clouds from that for clear-sky scenes to obtain tropospheric O_3. The drawback here is the requirement of a zonal invariance of stratospheric O_3, which is reasonably well fulfilled only in the tropics. In addition, the ozone column is obtained up to the cloud-top level, which is generally well below the tropopause.

In 1987, Fishman and Larsen (1987) proposed a residual technique that subtracts the stratospheric amount of O_3 from its total column using observations from different instruments since 1979 (tropospheric O_3 residual, TOR, technique). While the total O_3 column is retrieved from nadir measurements, its stratospheric contribution is obtained from limb observations providing O_3 profiles at a much higher vertical resolution (e.g. Ziemke et al., 1998; Fishman and Balok, 1999; Ladstätter-Weißenmayer et al., 2004; Ziemke et al., 2006; Schoeberl et al., 2007; Ziemke et al., 2011). The TOR technique generally provides global coverage. However, if limb and nadir instruments from different platforms are used, the stratospheric and total O_3 columns (locally separated) need to be averaged monthly or, in the best case, daily to achieve a global sampling which is similar to the CCD method.

Ebojie et al. (2014) were the first to use nadir and limb observations from the same instrument, SCIAMACHY (2002-2012), to obtain tropospheric ozone columns. The main advantage of this approach, referred to as the Limb-Nadir Matching (LNM), is that stratospheric and total ozone columns were obtained for nearly the same air mass, which was observed by SCIAMACHY in the limb and nadir viewing geometries within a few minutes. This technique minimizes the instrument-related bias and improves the spatiotemporal sampling.

Similar to SCIAMACHY, a combination of the Limb Profiler (LP) and Nadir Mapper (NM) instruments, which are parts of the Ozone Mapping and Profiler Suite (OMPS) on Suomi National Polar-orbiting Partnership platform (Suomi-NPP), provides the capability to observe the same air mass in limb and nadir geometries within a short time. Applying the LNM technique to the measurements from these instruments, tropospheric O_3 has been retrieved as described in this paper. Similar retrieval meth-

ods for stratospheric and total column ozone as for SCIAMACHY are applied to OMPS-LP and OMPS-NM measurements, respectively. The OMPS tropospheric ozone data set starting in 2012 can be merged with the 10-year tropospheric ozone time series from SCIAMACHY (2002-2012) to obtain a long-term data record of tropospheric ozone. This, however, will be a part

60 of a follow-up study.

The OMPS instrument, as well as the ozone column and profile data used in the TrOC retrieval, are presented in Section 2. The approach to obtain TrOC is described in Section 3. An extensive analysis of the uncertainty of the TrOC dataset is given in Section 4. The OMPS-LNM-TrOC data is evaluated in Section 5 by analysing global patterns and comparing with ozonesondes and two independent satellite datasets.

65 ## 2   Instrument and data used in the retrieval

OMPS is one of five instruments on board the Suomi-NPP satellite. The latter is a part of the Joint Polar Satellite System Program (JPSS), a collaborative program between the National Oceanic and Atmospheric Administration (NOAA) and the National Aeronautics and Space Administration (NASA) (Goldberg and Zhou, 2017). The satellite was launched on October 28th, 2011, into a sun-synchronous orbit with an ascending node at 13:30 local time at the equator. It flies at a mean altitude of

70 824 km (low-earth orbit) and performs about fourteen orbits per day.

OMPS comprises three instruments: Nadir Mapper (OMPS-NM), Nadir Profiler (OMPS-NP) and Limb Profiler (OMPS-LP). The detectors are focal plane arrays of two-dimensional charge-coupled devices with one spatial and one spectral dimension. OMPS-NM is a spectrometer designed to retrieve total column ozone. The spectrometer registers backscatter solar radiation from 300 to 380 nm, with a spectral resolution of 1 nm and a sampling of 0.42 nm. The footprint of OMPS-NM is approxi-

75 mately 50×2800 km^2, with a FOV of 0.27° ($\sim$ 50km) along-track and 110° across-track swath, divided into 36 bins (ground pixels). The across-track FOV is 20 and 30 km for the two central pixels, about 50 km for other near-central pixels and increases towards the edges of the across-track swath (Flynn et al., 2004, 2014; Seftor et al., 2014). A detailed instrument description can be found in Flynn et al. (2014).

The OMPS-LP instrument was designed to retrieve vertical ozone profiles in the upper troposphere and the stratosphere. It

80 makes observations with three vertical slits, the central one views along the satellite's orbital plane, and the other two sideways with their tangent points (TP) located approximately 250 km apart across-track. The central slit is aligned to observe the same air masses as in the nadir viewing geometry about 7 minutes behind. OMPS-LP performs 180 limb observations, referred to as states, per orbit from which around 140 are at solar zenith angles (SZAs) below 80°, which is used as the maximum SZA in the framework of this study. The horizontal sampling is about 3 km across-track and 150 km along-track. The spectral coverage

85 of OMPS-LP ranges from the UV (280 nm) to the NIR (1020 nm). The pixel columns of the charge-coupled ~~device performs instantaneous measurements of the entire atmosphere. Individual detector pixels~~ device observe the atmosphere vertically in 1 km steps ~~vertically~~ with a field of view of 1.5 km for each detector pixel. The pixel rows register the spectral distribution of the radiance at each tangent height.

This study uses the total ozone column (TOC) retrieved from OMPS-NM and OMPS-LP vertical ozone profiles to calculate the stratospheric ozone column (SOC). The retrievals were developed and performed at the Institute of Environmental Physics (IUP), University of Bremen.

2.1 OMPS-NM WFFA TOC

The Weighting Function Fitting Approach (WFFA) developed by us is employed to retrieve total ozone columns from OMPS-NM measurements (Orfanoz-Cheuquelaf et al., 2021)and is fully described in Orfanoz-Cheuquelaf et al. (2021). WFFA is a modification of the Weighting Function Differential Optical Absorption Spectroscopy (WFDOAS) technique, which is employed for the ozone total column retrieval from GOME, GOME-2, and SCIAMACHY (Coldewey-Egbers et al., 2005; Weber et al., 2022).

Similar to the WFDOAS technique, the WFFA algorithm approximates the measured atmospheric optical depth by a Taylor expansion around a first-guess atmospheric state. The main differences between the WFDOAS and WFFA are (Orfanoz-Cheuquelaf et al., 2021):

- A zero-degree polynomial is used instead of the cubic one (as in WFDOAS). This includes the broad-band spectral signature of ozone absorption in the fitting procedure.

- The spectral window is extended to 316-336 nm (in comparison to 325 to 335 nm in WFDOAS) to reduce the impact of the differential ozone absorption structure in the fit.

- Only the odd-numbered spectral points are used in the retrieval, counting from the first spectral point of the selected fitting window. This selection reduces the temperature dependency of the retrievalinfluence of the temperature weighting function within the fit procedure and makes the fit more stable.

The cloud fraction information is obtained from the operational OMPS-NM L2 product V2.1 from NASA (Jaross, 2017). The retrieval of effective cloud fraction is made using the Mixed Lambert Equivalent Reflectivity model, using a weak ozone absorption wavelength, 331.2 nm for most conditions, and 360 nm for large SZAs and high amounts of ozone (Seftor and Johnson, 2017).

The OMPS-WFFA TOC data was were validated by comparisons with collocated ground-based Brewer and Dobson measurements and four other satellite TOC datasets: OMPS NASA's product OMPS-NM L2 (McPeters et al., 2019)V2.1, OMI TOMS (McPeters et al., 2015), TROPOMI OFFL (Garane et al., 2019), and TROPOMI WFDOAS (Orfanoz-Cheuquelaf et al., 2021). Comparison of daily collocated data with ground-based measurements shows a mean bias below 1% for 21 out of 38 stations. For 20 stations, the standard deviations of the mean differences are under 3%. A mean bias of +0.5% and a standard deviation of 1.3% were found. All comparisons between OMPS-WFFA TOC and other satellite products are consistent with respect to the seasonality and variability with latitude. OMPS WFFA TOC presents a zero yearly global mean bias with respect to OMPS L2 product of NASA, approximately 0.7% with respect to OMI TOMS, -0.8% with respect to TROPOMI OFFL and -2.4% with respect to TROPOMI WFDOAS. The standard deviations of the differences are around 1.7% for all

4

satellite validation datasets, except for OMI TOMS, for which the standard deviation reaches 3.0%. Larger differences were found for polar regions and larger SZAs. Details on the WFFA retrieval algorithm and validation of the results can be found in Orfanoz-Cheuquelaf et al. (2021).

2.2 IUP dataset of stratospheric ozone profiles from OMPS-LP

125 The algorithm for retrieving limb ozone profiles (Arosio et al., 2018; Arosio, 2019) employs the ~~regularized~~ regularised inversion technique with the first-order Tikhonov constraints (Rodgers, 2000) and is similar to the SCIAMACHY algorithm (Jia et al., 2015). ~~In this study, OMPS ozone profiles version 3.3 are used.~~ Depending on altitude, the ozone profile retrieval uses different spectral ranges of the OMPS-LP L1 ~~version 2.5~~ data. For higher tangent heights (TH), three spectral segments in the UV range are selected, while for the lower stratosphere, the visible (VIS) spectral range is used. ~~Table 1 lists TH segments,~~
130 ~~respective spectral ranges selected for the retrieval, and THs used for the spectral normalization~~ Radiances are normalized using an upper TH measurement. A polynomial is subtracted from the spectrum as a part of the overall fitting procedure ~~in the two lowermost THsegments. The order of the polynomials is also listed in the table. Further~~ . Clouds in the instrument field of view are detected using the Color Index Ratio (CIR) concept described in Eichmann et al. (2016). The ratio between two radiances at wavelengths with weak ozone absorption (754 and 868 nm), called the Color Index (CI), is calculated for every TH. The
135 CIR is defined as the ratio of the CI at two neighbouring THs. For CIR higher than 1.08, the tangent height is marked as cloudy.

This study uses OMPS ozone profiles version 3.3 (IUP-OMPS V3.3). Comprehensive validation of the ozone profiles and details about the ~~OMPS~~ retrieval can be found in Arosio et al. (2018) and Arosio (2019) ~~.~~ for the previous retrieval version (here named IUP-OMPS V2.6). The main differences between V2.6 and V3.3 are in the usage of the spectral segments
140 and normalization THs. Table 1 lists the TH ranges, respective spectral segments selected for the retrieval, TH used for the normalization, and the order of the polynomials used for V3.3. Figure 1 presents a comparison of ozone profiles from Microwave Limb Sounder (MLS) with IUP-OMPS V2.6 (left panel) and V3.3 (right panel) data. Both panels show relative differences between IUP-OMPS and the MLS L2 version 4.2 data as a function of altitude and latitude. Differences within ±10% are observed above 20 km for both IUP-OMPS versions. Below 20 km, the differences can reach ±30%. An overall
145 reduction of the bias is found for IUP-OMPS V3.3, with main improvements in the lower tropical stratosphere and between 35 and 50 km. However, the bias increases between 30 and 35 km from 20°N to the south and below 20 km polewards of 60°S. ~~Because of long-term stability issues in the recent years, the~~ The OMPS-LP ozone profile time series based on ~~level 1~~ L1 V2.5 data ~~are trusted only until 2018.~~ , which are used by both V2.6 and V3.3 retrievals, were found to exhibit a significant positive drift after 2018 (Kramarova et al., 2018). For this reason, only the data until 2018 are used to create the OMPS-LNM-TrOC
150 dataset. Currently, only measurements from the central slit are used to retrieve ozone profiles because of remaining calibration issues related to the measurements from the side slits. More information and technical details on OMPS-LP can be found in Kramarova et al. (2018), Arosio et al. (2018), and references therein.

~~A comprehensive validation of ozone profiles from the previous retrieval version (IUP-OMPS V2.6) was presented in Arosio et al. (2018). In Fig. 1, a comparison with ozone profiles from Microwave Limb Sounder (MLS) is shown for IUP-OMPS~~

Table 1. Details of the IUP-OMPS ozone profile retrieval V3.3: TH segments, corresponding spectral ranges, and the order of the subtracted polynomial (dash means that no polynomial is subtracted). Tangent heights TH_{norm} are used to normalise the radiance in the given spectral range.

TH segment [km]	Spectral range [nm]	TH_{norm} [km]	Polynomial degree
48 - 60	290 - 302	63.5	-
34 - 49	305 - 313	51.5	-
28 - 39	321 - 330	48.5	0
12 - 31	508 - 585	43.5	1
	600 - 628		
	630 - 660		

155 ~~V2.6 (left panel) and V3.3 (right panel) data. Both panels show relative differences between IUP-OMPS and the MLS L2 version 4.2 data as a function of altitude and latitude. Differences within ±10% are observed above 20 for both IUP-OMPS versions. Below 20 , the differences can reach ±30%. The main improvement is found in the lower tropical stratosphere, where V3.3 shows a better agreement with MLS. The bias increases between 30 and 35 from 20°N to the south and below 20 polewards of 60°S.~~

2.3 Tropopause height

In order to derive the stratospheric column from the retrieved ozone profile, the tropopause height (TPH) needs to be determined. The stratospheric column is then calculated by integrating the ozone profile from the tropopause up to the top-of-atmosphere; here, to the uppermost retrieval altitude of 60.5 km.

The most commonly used definition of the tropopause is the thermal or lapse-rate tropopause. WMO (World Meteorological Organization) (1957) defines the thermal TPH as the lowest altitude level at which the lapse rate is less or equal to 2 K/km, provided also the average lapse rate between this level and all higher levels within 2 km does not exceed this threshold. A drawback of this definition is that it might fail in polar regions if the stratosphere is very cold. Alternatively, the dynamic tropopause can be used, which is defined by the potential vorticity (PV), which increases with altitude. Different studies suggest this tropopause altitude to be between 1 and 4 PVU (potential vorticity unit, $1PVU = 1.0 \times 10^6$ km^{2}kg^{-1}s^{-1}) (Hoinka, 1998). This tropopause definition is, however, only applicable in the extra-tropics.

In this study, a blended tropopause definition is employed: the thermal tropopause is used in the tropics, between 20°N and 20°S, while the altitude level with a PV of 3.5 PVU (Zängl and Hoinka, 2001) is selected as TPH for latitudes above 30°. In the transition zone, between 20° and 30° latitude in each hemisphere, the TPH is calculated by averaging the thermal and the dynamical values weighted with the distance to the regime boundaries. This approach is consistent with the TPH definition
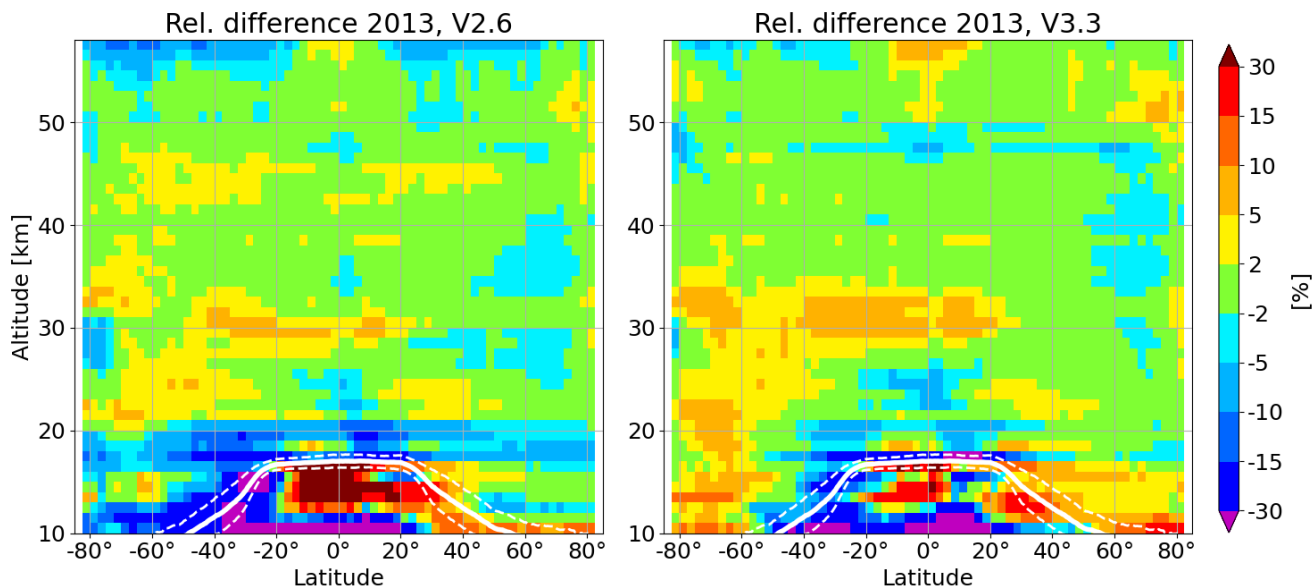
6

Figure 1. Relative mean differences between IUP-OMPS and MLS version 4.2 ozone profiles as a function of altitude and latitude ~~.~~ for 2013. The left panel shows the comparison for IUP-OMPS V2.6 and the right panel for IUP-OMPS V3.3. The thick white line marks the tropopause height; the dashed line its standard deviation.

employed in Ebojie et al. (2014) and Jia (2016) to obtain tropospheric ozone from SCIAMACHY using the Limb-Nadir Matching technique.

For every IUP-OMPS ozone profile location and time, the thermal and the dynamic TPHs are determined using the ECMWF ERA-5 reanalysis data (Hersbach et al., 2020)~~with~~. The ECMWF ERA-5 data has a spatial resolution of 0.75~~° ×°~~$\times$0.75° and a temporal sampling of six hours. The data is linearly interpolated using the four data points around the exact given location for the two closest times to obtain the TPH at the precise time and place of every limb state.

3 Obtaining tropospheric ozone columns from OMPS-NM/OMPS-LP LNM

Employing the LNM technique, the tropospheric ozone product is generated for matched observations as follows:

$$\text{TrOC} = \text{TOC} - \text{SOC}. \tag{1}$$

This means that the SOC, calculated from IUP-OMPS ozone profiles, is subtracted from TOC, retrieved from OMPS-NM using the WFFA approach. The latter retrieval is done only for those across-track ground pixels that are collocated to the location of the TP of the limb ozone profiles (usually around the centre of the swath). Both retrievals are completely independent of each

7

other. For a consistency reason, they use thesame ozone absorption cross-sections, Serdyuchenko et al. (2014). Details on the matching procedure, which identifies the collocated ground pixels, are given below.

Although the IUP-OMPS ozone profiles are available from 8.5 km to 60.5 km altitude, only ozone values above 12.5 km are considered because of a ~~larger~~ large retrieval uncertainty of the limb ~~observations~~ profiles below this altitude (Arosio et al., 2018). If the TPH calculated as described in section 2.3 is below 12.5 km, the ozone vertical distribution between TPH and 12.5 km is taken from the IUP-2018 ozone profile climatology (Orfanoz-Cheuquelaf et al., 2021). This climatology classifies ozone profiles as a function of season, latitude, and total ozone column. The climatological profile is offset by a scalar value which is given by the difference between the observed and climatological ozone at 12.5 km.

Subsequently, cloud flags provided along with the ozone profiles are analyzed. The complete profile is rejected if clouds above the TPH are detected. After passing the cloud filter, a vertical resolution quality filter is applied, which considers the mean and the standard deviation of the vertical resolutions of all profiles observed within a given calendar year. If the vertical resolution of a single ozone profile at any altitude between 12.5 and 60.5 km deviates by more than two standard deviations from the yearly mean, the entire profile is rejected.

The SOC in DU is determined then by integrating the O_3 concentration from the TPH to 60.5 km, as follows:

$$\text{SOC} = \frac{1}{2} \sum_{i(\text{TPH})}^{i(60.5\text{km})-1} \frac{(c_{i+1} + c_i)(z_{i+1} - z_i)}{2.6867 \times 10^{11}}, \tag{2}$$

where i is the index of the altitude level, c the ozone number density in units of $\text{molecules}/\text{cm}^3$, and z the altitude in units of km.

The LNM procedure is illustrated in Fig. 2. The grid cells plotted in the figure correspond to the ground pixels of OMPS-NM, and the red points represent the tangent height footprint of the OMPS-LP states. The matching is done as follows. For each OMPS-LP state location (red points), the OMPS-NM ground pixel ~~is identified, which~~ that contains the location of TPs is identified (orange box in Fig. 2). ~~Two~~, and two neighbouring across-track pixels (yellow boxes) are also selected ~~. In addition, the~~ to obtain a mean TOC. The matching procedure also considers all triple pixels between consecutive limb states (e.g., a row of three yellow boxes). ~~The final TOC is obtained by averaging the three OMPS-NM across-track pixels around the location of the OMPS-LP state.~~ If the OMPS-NM pixels are located between consecutive OMPS-LP states, the final SOC value to be subtracted is obtained by interpolating between the SOCs from the two bracketing limb states. Finally, the subtraction SOC from TOC is performed to yield TrOC. The final size of the TrOC pixels is approximately 50 km along-track and 150 km across-track. For the calculation of the three-pixel mean TOC, only cloud-free OMPS-NM pixels (cloud fraction below 0.1) are used to calculate the three-pixel mean TOC. If a single cloudy pixel is detected, this one is neglected, and the average is performed. The entire matching is rejected in case of two or more cloudy TOC pixels.
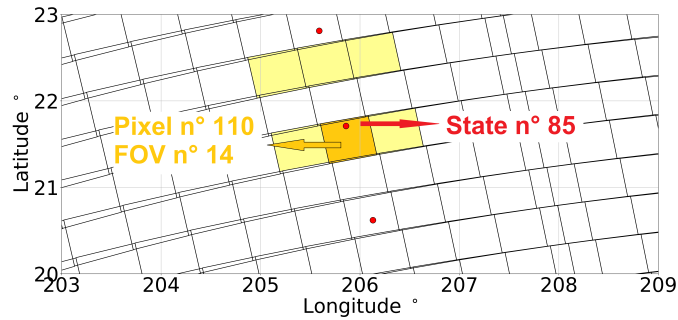
Figure 2. Example of ~~a~~ the matching between OMPS-NM and OMPS-LP observation scenes. The red points mark the footprints of tangent ~~height footprint~~ points (TPs) of the limb observations. The grid cells represent the ground pixels of OMPS-NM. The yellow ~~and orange~~ boxes indicate the nadir ground pixel averaged to obtain the TOC assuming the nadir pixels are cloud-free. The orange box marks the exact match between the OMPS-NM ground pixel number 110 (along-track) in position 14 (across-track) with the OMPS-LP observation number 85 (state).

4 OMPS-LNM uncertainties

Uncertainties from the ozone total column and profile retrievals contribute to the uncertainty of the tropospheric ozone data. An additional contribution comes from the uncertainty in the tropopause height calculation. The overall TrOC uncertainty is estimated by combining these three components in a Gaussian sum as follows:

$$X_{\text{TrOC}} = \sqrt{X_{\text{TOC}}^2 + X_{\text{SOC}}^2 + X_{\text{TPH}}^2}, \tag{3}$$

where X_{TrOC}, X_{TOC}, X_{SOC} and X_{TPH} are the uncertainties estimated for the tropospheric ozone column, total ozone column, stratospheric ozone column, and tropopause height, respectively, all expressed in DU. All values reported in this section are assumed to be 1-σ uncertainties and represent the uncertainty of a single observation.

The analysis in this study distinguishes between random and systematic uncertainties, with random components contributing to the variance of the data and systematic components contributing to the bias. In the following, details on the terms on the right-hand side of Eq. 3 are discussed.

4.1 Total ozone column uncertainty

The full analysis of uncertainties related to the WFDOAS technique is detailed in Coldewey-Egbers et al. (2005). Due to differences in the spectral window size and the polynomial degree, the uncertainty analysis was repeated for the WFFA technique for some parameters as reported in Orfanoz-Cheuquelaf et al. (2021). For some other parameters, the uncertainties derived from the WFDOAS technique were ~~considered to be~~ also considered valid for WFFA~~as well~~. Table 2 summarises individual contributions to the overall TOC uncertainty from the analysis presented in Coldewey-Egbers et al. (2005) and Orfanoz-Cheuquelaf et al. (2021).

Table 2. Summary of contributions to the uncertainty of the total ozone column.

Source	TOC uncertainty ~~, %~~ [%]
~~Tropospheric ozone increase~~ Enhanced a-priori tropospheric ozone profile[1]	< 0.01 ~~%~~
Ozone absorption cross-section[1]	< 1 ~~%~~ below 70° SZA
	1-2 ~~%~~ beyond 70° SZA
Enhanced non-absorbing aerosols[1]	1-2 ~~%~~ below 50° SZA
	∼ 0.5 ~~%~~ beyond 50° SZA
Enhanced absorbing aerosols[1]	< 1 ~~%~~ below 50° SZA
	2-3 ~~%~~ beyond 50° SZA
O_3 and T a-priori profiles[2]	1 ~~%~~ below 80° SZA
	5 ~~%~~ beyond 80° SZA
Pseudo-spherical approximation[2]	0.3 ~~%~~

(1) Orfanoz-Cheuquelaf et al. (2021), (2) Coldewey-Egbers et al. (2005).

In particular, for ~~an increase in~~ the case of increasing the tropospheric ozone a-priori profile by a factor of five, the uncertainty in TOC is less than 0.01%. For different absorption cross-sections (BDM (Malicet et al., 1995) vs Serdyuchenko (Serdyuchenko et al., 2014)), the uncertainty is less than 1% for SZAs below 70° and increases to 2% for higher SZAs. For scenes with enhanced boundary layer aerosols at SZAs below 50°, the uncertainties are between 1 and 2% for non-absorbing aerosols and less than 1% for absorbing aerosols. For SZAs beyond 50°, the uncertainties are about 0.5% for non-absorbing aerosols and between 2 and 3% for absorbing aerosols. For ozone and temperature a-priori profiles, the uncertainty is 1% for SZAs under 80°. The use of the pseudo-spherical approximation results in an uncertainty of 0.3%.

From the contributions listed in Table 2, the only systematic component is the uncertainty associated with the absorption cross-section, which results in a systematic uncertainty of TOC of about 1%. The total random component is calculated by summing up all other contributions using the Gaussian rule. This results in a random uncertainty of 1.8 - 3.8%, where the range is mostly dominated by the aerosol scenarios, particularly in extreme cases. A typical random uncertainty is estimated to be about 2.8%. For a typical total ozone amount of about 300 DU (Rowland et al., 1988), the random uncertainty of 2.8% translates into 8.4 DU, and the systematic uncertainty of 1% into 3 DU.

4.2 Stratospheric ozone column uncertainty

A comprehensive discussion of the uncertainty budget for the IUP-OMPS ozone profiles was presented by Arosio et al. (2022). Uncertainties due to retrieval noise and from the retrieval parameters, i.e. parameters that do not enter the measurement vector, are quantified using synthetic retrievals and extensively discussed in the above mentioned study. Uncertainties originating from model approximations and spectroscopic data are also investigated. A representative set of OMPS-LP geometries was selected to provide a reliable estimation of the uncertainties as a function of latitude and season.
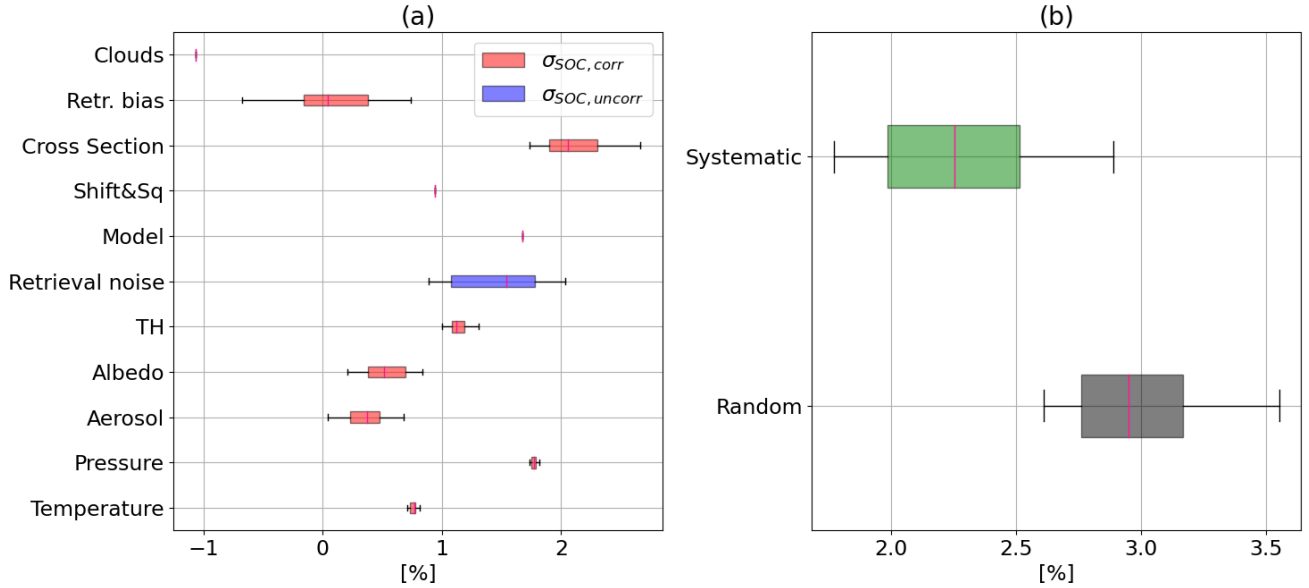
Figure 3. Contributions to SOC uncertainty. Panel (a): SOC uncertainties from different sources. Panel (b): total random and systematic uncertainty for SOC. The error bars span the outlier ranges, the boxes span between the first and third percentiles, and the magenta middle lines refer to the median values.

To assess the SOC uncertainty based on the available uncertainty budget for ozone profiles, first, we need to discuss the behaviour of the uncertainty components in the altitude domain. In this study, we consider the uncertainties of the pressure,

255 temperature and aerosol extinction coefficient to be predominantly systematic in the altitude domain. This is because the former two parameters are taken from the GEOS-5 model data, whose uncertainties originate from the model assumptions with more probable large-scale influence rather than from random noise-like errors. Concerning the stratospheric aerosol extinction coefficients, our experience is that dominating errors in their retrievals mostly scale the resulting vertical profiles. The retrieval-noise-related uncertainty is considered uncorrelated with altitude, i.e. is randomly distributed in the vertical domain. As a

260 consequence, the following formulas have been used to calculate the SOC uncertainty from the profile values:

$$\sigma_{SOC,correlated} = \sum_z \sigma_{O_3}(z) / \sum_z O_3(z) \tag{4}$$

$$\sigma_{SOC,uncorrelated} = \sqrt{\sum_z (\sigma_{O_3}(z))^2} / \sum_z O_3(z), \tag{5}$$

where O_3 and σ_{O_3} are, respectively, the reference ozone concentrations and their uncertainties as functions of altitude z. The second equation was applied only for the uncertainty from retrieval noise.

265 The SOC uncertainty contributions estimated from a selected representative set of geometries (Arosio et al., 2022) are shown in panel (a) of Fig. 3, where different colours indicate the usage of Eq.4 (blue) or Eq.5 (red), respectively. Uncertainties related

to the cloud impact, the radiative transfer model, and the use of the spectral shift/squeeze correction in the pre-processing routine ('Shift&Sq') are independent of the viewing geometry, so that a single value is available. For other contributions, the statistics within the data sample are shown. The contribution from cloud artefacts is based on Fig. 10a of Arosio et al. (2022), assuming that thin tropospheric clouds can still affect the retrieval bypassing the 0.1 cloud fraction threshold imposed on the nadir pixel (total column ozone) in the matching procedure.

The total random SOC uncertainty was calculated by applying the Gaussian sum:

$$\sigma_{SOC,random} = \sqrt{\sigma^2_{SOC,P} + \sigma^2_{SOC,T} + \sigma^2_{SOC,alb} + \sigma^2_{SOC,aer} + \sigma^2_{SOC,TH} + \sigma^2_{SOC,ret.noise} + \sigma^2_{SOC,S\&S}}$$

(6)

where the various terms on the right-hand side denote the individual components related to the retrieval parameters, i.e. pressure ($\sigma_{SOC,P}$), temperature ($\sigma_{SOC,T}$), surface albedo ($\sigma_{SOC,alb}$), aerosol extinction ($\sigma_{SOC,aer}$) and TH ($\sigma_{SOC,TH}$) correction, and to both the retrieval noise ($\sigma_{SOC,ret.noise}$) and the shift and squeeze correction ($\sigma_{SOC,S\&S}$).

The total systematic uncertainty was computed as follows:

$$\sigma_{SOC,systematic} = \sqrt{(\sigma_{SOC,retr.\ bias} + \sigma_{SOC,clouds} + \sigma_{SOC,model})^2 + \sigma^2_{SOC,cross\ section}}$$

(7)

where the terms with known signs are first summed up, i.e. the uncertainties related to the retrieval bias ($\sigma_{SOC,retr.\ bias}$), cloud artefacts ($\sigma_{SOC,clouds}$), and radiative transfer model approximations ($\sigma_{SOC,model}$). Finally, the root mean square with the cross section term ($\sigma_{SOC,cross\ section}$) is calculated.

The total systematic and random SOC uncertainties are illustrated in panel (b) of Fig. 3. Their typical values are about $2.0 - 2.5\%$ and $2.8 - 3.2\%$, respectively. The median of 2.2% for the systematic and 3% for the random uncertainties are used below to calculate the final uncertainty of TrOC. Considering that stratospheric ozone contributes approximately 90% to the total ozone, and the global average of the total ozone is 300 DU, the global average of SOC is about 270 DU. Thus, the systematic uncertainty of 2.2% translates to 5.9 DU, and the random uncertainty of 3% to 8 DU.

4.3 Tropopause height uncertainty

The calculated TPH introduces another uncertainty in the retrieved TrOC. Besides the natural variability of the TPH and the particular definition used to determine it, the uncertainty depends on the vertical resolution of the reanalysis data used to determine TPH, here ECMWF ERA-5 dataset. The ERA-5 reanalysis data is provided at pressure levels, and derived quantities as the PV are defined at the centre of the layers bordering the pressure levels. To determine the tropopause altitude in km, the pressure levels are converted into geometrical heights. In this domain, the vertical sampling of the ERA-5 dataset varies with altitude ranging from 270 to 400 m between 5 and 20 km altitude.

The TPH uncertainty as a function of latitude is determined by the vertical extent of the ERA-5 layer containing the TPH and is estimated using the zonal mean (climatology) of the TPH to be 0.29 km in the northern hemisphere, 0.33 km in

Table 3. Uncertainties related to TPH for the northern hemisphere, tropics, and southern hemisphere.

Latitude range	TPH [km]	TPH uncertainty [km]	TrOC uncertainty [DU]
NH (30°N-60°N)	8.7-14.4	0.29	0.8 - 2.0
Tropics (30°S-30°N)	14.2-17.0	0.33	0.6 - 0.8
SH (30°S-60°S)	8.2-13.9	0.29	0.8 - 1.3

Table 4. Estimated uncertainties for TOC, SOC, TPH and TrOC.

Component	TOC uncertainty [~~DU~~DU]	SOC uncertainty [~~DU~~DU]	TPH uncertainty [~~DU~~DU]	**TrOC uncertainty [~~DU~~DU]**
Systematic	3.0	5.9	-	**6.5**
Random	8.4	8.0	0.6 - 2.0	**12**

the tropics and 0.29 km in the southern hemisphere. To calculate the effect on TrOC, these uncertainties were added to and subtracted from the TPH in the OMPS-LNM processing chain. The TPH range, their uncertainties, and the final contributions to the TrOC uncertainty are presented in Table 3 for three zonal bands. In the northern hemisphere (NH), the mean uncertainty in TrOC ranges from 0.8 to 2 DU, in the tropics, from 0.6 to 0.8 DU, and in the southern hemisphere (SH) between 0.8 and
300   1.3 DU.

4.4   Final tropospheric ozone column uncertainties

The systematic and random components of the final TrOC uncertainty are calculated using Eq. 3 and the results are summarised in Table 4. The TPH contribution is considered random. Although a range of values was obtained for the TPH uncertainty, this variation does not impact the final results. The final TrOC uncertainties do not vary significantly with latitude. The overall
305   random and systematic uncertainties of OMPS-LNM TrOC are about 12 DU and 6.5 DU, respectively.

The standard Level 3 product of the OMPS-LNM is a monthly mean gridded ($0.5° \times 1.5°$ (latitude/longitude)) dataset. The overall uncertainty for a typical Level 3 data point can be estimated as follows:

$$\sigma_{TrOC_{L3}} = \sqrt{X_{TrOC_{syst}}^2 + \frac{X_{TrOC_{random}}^2}{N}}, \tag{8}$$

where N is ~~a typical~~ the number of observations averaged within a ~~typical grid cell. In our case~~ grid cell; in our case, it is about
310   14. The total uncertainty for a typical Level 3 data point is then estimated to be 7.2 DU. The corresponding uncertainties in percentage are provided in Table A1 for representative TrOC values of 20, 30, and 40 DU.
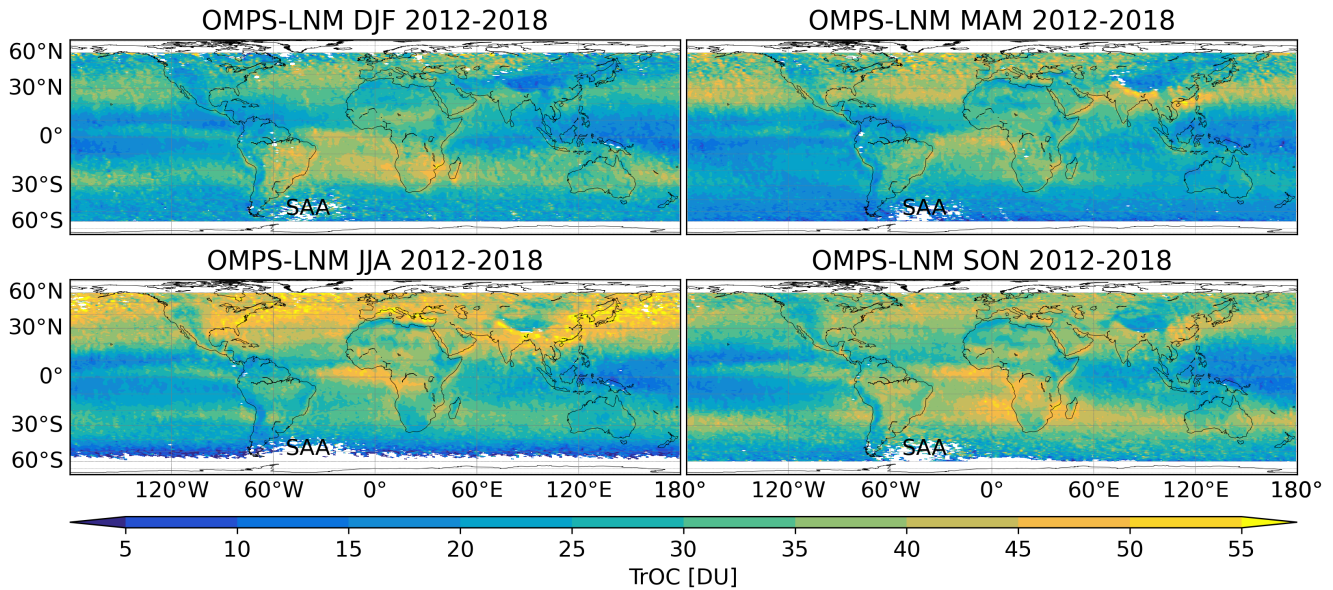
Figure 4. Seasonal maps of OMPS-LNM TrOC averaged from 2012 to 2018.

5 OMPS-LNM tropospheric ozone evaluation

In this section, the OMPS-LNM TrOC dataset is described and compared with ozonesondes and other satellite datasets, here OMI/MLS TOR and TROPOMI CCD. For the evaluation, the OMPS-LNM TrOC data were ~~binned into a~~ mapped onto a

315   regular daily grid of ~~0.5° × 1.5°~~ 0.5°×1.5° (latitude/longitude) from 60°S to 60°N.

5.1 Seasonal analysis

Figure 4 shows seasonal maps of OMPS-LNM TrOC. The region of the South Atlantic Anomaly (SAA) is marked on the map. This is an anomaly of the Earth's geomagnetic field (Pavón-Carrasco and De Santis, 2016) that affects satellite electronics and perturbs measurements. After applying the quality filters, the data density is significantly reduced within the SAA.

320   A band of higher values is observed between 0° to 10°N in the Pacific Ocean during all seasons and in the Atlantic Ocean during boreal summer (JJA) and autumn (SON). This feature is not seen in other satellite datasets and will be discussed in more detail in Section 5.2.

The seasonal tropospheric ozone maps show, apart from the above mentioned issue, typical features reported before. Higher values in the extratropical hemispheric spring/summer are observed, coinciding with the likely increase in the photochemical

325   production of tropospheric ozone ~~(Logan, 1985)~~(Logan, 1985; Monks et al., 2015; Gaudel et al., 2018). Low ozone is observed throughout the year in high-topography areas like the Andes and the Himalayas. Minimum ozone is observed above Indonesia, extending into the Pacific Ocean.

14

Most of the year, high values are observed in the southern subtropical Pacific Ocean (20°S-30°S), attributed to biomass burning and stratospheric intrusions (Daskalakis et al., 2022). Higher values are observed above East Asia and the northern

330 subtropical Pacific in all seasons, with maxima during boreal spring/summer. In addition to increased photochemical production of ozone during spring/summer, these high values might be caused by stratospheric intrusions above the ocean around 30°N (Oltmans, 2004) and outflow from intensive biomass burning in continental Southeast Asia contributing during winter and spring (Liu et al., 1999).

High values, largest during boreal summer and lower during boreal autumn/winter, are observed over the subtropical North

335 Atlantic throughout the year. During winter, high values are associated with the long-range transport of precursors from anthropogenic emissions in North America (Cuevas et al., 2013). In addition to ~~the~~ photochemical production, stratospheric intrusions ~~are also an important contributor~~ (Škerlak et al., 2014) and lighting (Cooper et al., 2009) are important contributors during the summer~~(Škerlak et al., 2014)~~. Over the tropical Atlantic Ocean, lightning contributes to tropospheric ozone increase (Jenkins and Ryu, 2004). During austral spring/summer, the maximum over the southern Atlantic Ocean results from contributions of

340 biomass burning in Africa and South America, as well as from NO_x soil sources (Sauvage et al., 2007). High values above the South Indian Ocean are associated with biomass burning in Africa, particularly during austral spring, in addition to stratospheric intrusions (Fishman et al., 1991; Liu et al., 2017). The seasonality observed over the Arabian Sea is consistent with the analysis presented by Jia et al. (2017).

5.2 Band of high ozone over the northern tropical Pacific and Atlantic oceans

345 A band of fairly high tropospheric ozone columns over the Pacific and Atlantic oceans is seen in OMPS-LNM data between the Equator and 10°N. Such a band is not observed by satellite datasets which use nadir ozone profiles (Ohyama et al., 2012), the CCD method (Valks et al., 2014; Leventidou et al., 2016; Hubert et al., 2021), or residual techniques employing occultation or limb-emission measurements (Fishman et al., 2003; Ziemke et al., 2006). However, this particular feature is observable in the LNM dataset from SCIAMACHY (Jia, 2016) and in the NASA product from OMPS (Ziemke, 2019). This indicates that it

350 is most likely a feature specific to the residual technique employing limb-scatter measurements.

Figure 5 shows maps of TOC and SOC anomalies from the OMPS-LNM TrOC analysis between 20°S and 20°N. The anomalies were computed by subtracting the ~~mean value~~ long-term mean from all data in the tropics. The SOC anomalies (Fig. 5a) show lower values over the Pacific and Atlantic, matching the band of high TrOC (Fig. 4). This feature is not evident in the TOC anomalies (Fig. 5b). A seasonal analysis of the SOC anomalies (not shown here) shows that this feature is per-

355 sistent throughout the year, only slightly weaker during boreal summer. The negative bias in SOC leads to a high bias in the tropospheric ozone of about 10 DU (see Fig. 4). We conclude that this feature is likely an artefact from the limb ozone profiles.

Among other parameters, the surface reflectivity field retrieved along with the ozone profiles from OMPS-LP was analysed to investigate the cause of the unusually low OMPS-LP SOC. An area with higher surface reflectivity between the Equator and 10°N over the Pacific and Atlantic oceans correlates with the anomalous band. The enhanced surface albedo band is shifted a

360 few degrees northwards and is somewhat wider than the tropospheric ozone and SOC anomaly bands. The enhanced surface reflectivity band matches the position of the Inter-Tropical Convergence Zone (ITCZ). Even though the LNM tropospheric
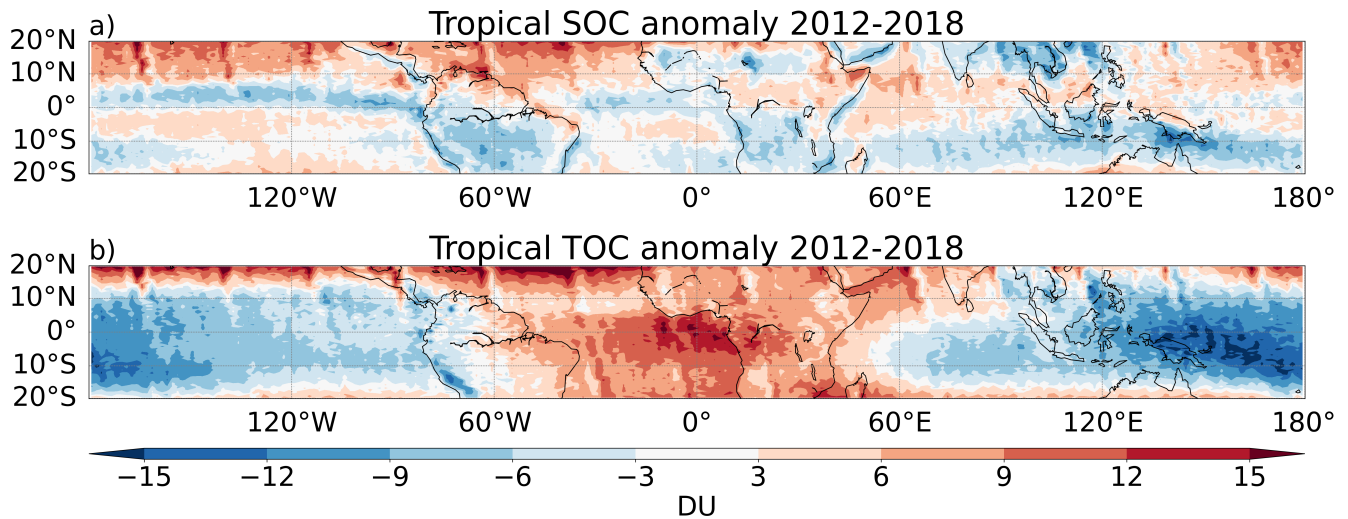
Figure 5. OMPS-LNM tropical anomalies of ~~TOC (top~~a) ~~and~~ SOC and (~~bottom~~b) TOC from 2012 to 2018.

ozone used only ozone profiles free of clouds above the tropopause and nadir pixels with cloud fraction below 0.1, the influence of the ITCZ on TrOC is evident.

Figure 6 shows the latitudinal dependence of the July-September 2016 average SOC over the Pacific Ocean from ~~OMPS~~
365   OMPS-LP (red) and MLS (black), the cloud-top-height (green) from OMPS-LP and the surface reflectivity (blue) retrieved from OMPS-NM. It is seen that the cloud top height significantly increases north of the Equator, and the reflectivity increases as well. A correlation between OMPS SOC and the reflectivity gradient is observed. When the gradient in the reflectivity is maximum, the OMPS SOC reaches a minimum, decreasing by around 10 DU relative to MLS. OMPS SOC recovers rapidly as the gradient in the reflectivity changes. The MLS SOC does not show any dependence on the presence of clouds. ~~A similar~~
370   ~~behaviour was observed over the Atlantic Ocean (not shown here).~~

In a more extensive comparison between SOC from OMPS-LP and MLS, Fig. 7 shows the global difference between the datasets for the entire period 2012-2018. The band of lower SOC from OMPS-LP in the Pacific and Atlantic oceans is clearly seen. Also, a larger difference is observed between Australia and the Equator. Larger OMPS-LP values are seen in the Southern Mediterranean Sea and in the transition zone between the bright desert and the dark sea. The current hypothesis is that a strong
375   gradient in the surface reflectivity along the instrument Line-of-Sight (LOS) is not properly accounted for in the limb retrieval and generates artefacts in the retrieved ozone profiles. This affects all limb-scatter retrievals: IUP-OMPS, SCIAMACHY and NASA OMPS-LP. An investigation of the influence of the horizontal gradient in the reflectivity of the underlying scene on one-dimensional limb profile retrievals is out of the scope of this research. However, it is important to be aware of this influence on the OMPS-LNM tropospheric ozone.
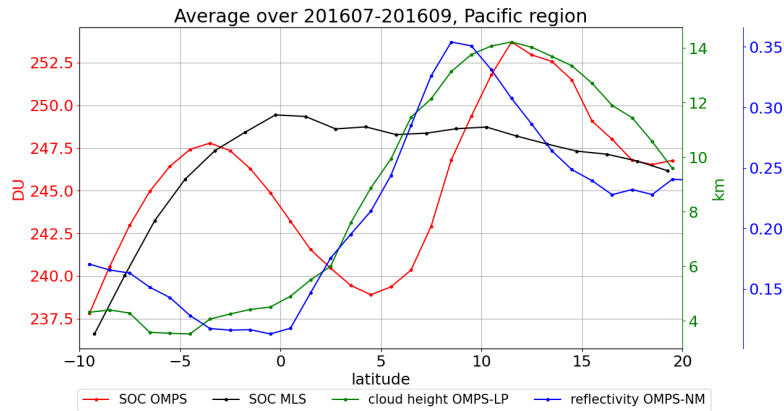
Figure 6. Latitudinal dependence of the July-September 2016 SOC average over the Pacific Ocean ~~of~~ from OMPS (red) and MLS (black), the mean cloud-top-height (green) and mean surface reflectivity (blue).
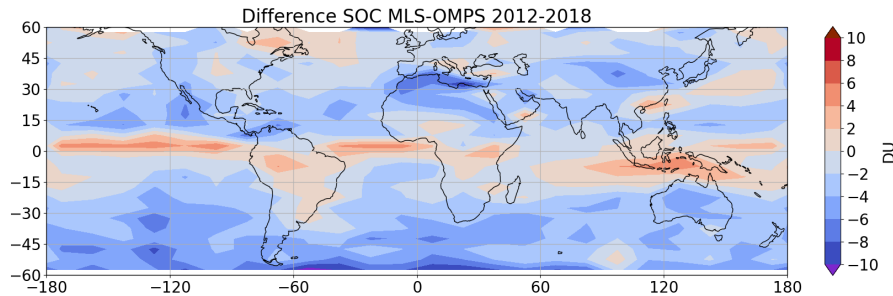

Figure 7. Mean differences in SOC from MLS and IUP OMPS-LP profiles from 2012 to 2018.

5.3 Comparison with ozonesondes

Ozonesonde data from WOUDC (Fioletov et al., 1999) and SHADOZ V6 (Witte et al., 2017; Thompson et al., 2017) were used in this study. The procedure to create collocated OMPS-LNM dataset was optimized to obtain a sufficient number of comparisons. For each ozonesonde profile, OMPS-LNM data from the grid cell enclosing the launch site and all immediately adjacent grid cells were averaged (without any weighting) to create the collocated OMPS dataset. The temporal averaging included OMPS-LNM data from the day of the ozonesonde launch, one day before, and one day after the launch. Only ozonesonde sites with collocated OMPS data of at least 55 days during the entire comparison period (2012-2018) were considered. In total, 22 sites were available, eight from SHADOZ and fourteen from WOUDC. The total number of collocated days is rather low for seven years because the daily coverage of OMPS-LNM is sparse, and ozonesondes are launched four times per month at maximum.
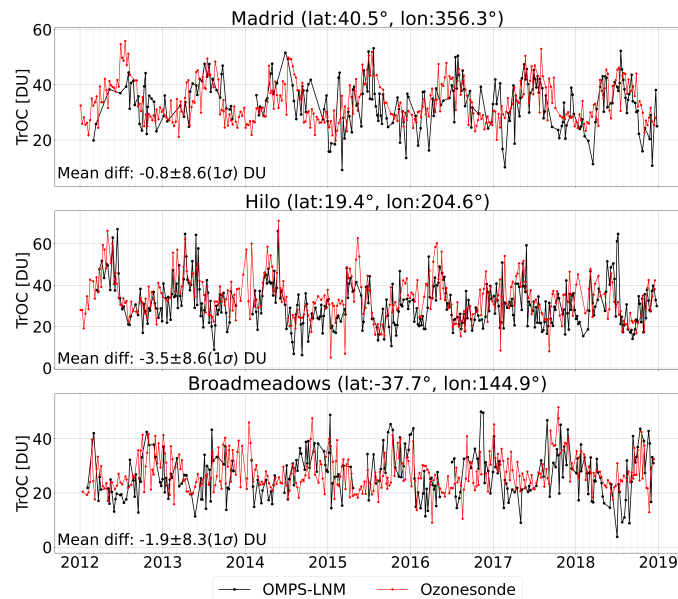
17

Figure 8. Time series of tropospheric ozone column from ~~ozonesondes~~ individual ozonesonde measurements (red) and daily averaged collocated OMPS-LNM (black) data for three selected sites.

Figure 8 shows time series of ~~collocated~~ ozonesonde (red) and collocated OMPS-LNM (black) tropospheric ozone columns for three selected sites: Madrid in the northern hemisphere (40.5°N, 3.7°W), Hilo in the tropics (19.4°N, 155.4°W) and Broadmeadows in the southern hemisphere (37.7°S, 145°E). The seasonality and variability shown by both datasets are in good agreement. The bias between the datasets is -0.8, -3.5 and -1.9 DU, respectively, with OMPS-LNM being generally lower than the sondes. The standard deviation of the difference is around 8.5 DU for each site. No clear dependence on latitude is identified from the analysis of differences between the OMPS-LNM and ozonesonde data for all sites (not shown here).

Table 5 summarises the ~~mean value and standard deviation of the collocated data~~ collocated mean value from the ozonesondes and OMPS, their standard deviation, and the mean difference (average of OMPS-LNM ~~- Ozonesonde~~ minus Ozonesonde time series) between the datasets for all ~~compared~~ sites. The table's first column shows the site's name and the number of collocated days. No dependency on the number of collocated days is observed. Typically, the standard deviations for OMPS-LNM are higher than those for ozonesondes by about 2.7 DU. Larger differences in the standard deviation are found for Yarmouth, Lauder, and Macquarie Island, where the standard deviations of OMPS-LNM are higher than those of the ozonesondes by 7.3, 6.6 and 6.6 DU, respectively. Some exceptions are Hilo, Natal, and Irene, where the standard deviations of the ozonesondes are higher than those for OMPS-LNM by 0.5, 0.3, and 0.5 DU respectively. The standard deviations of the differences range from 6.4 DU for Nairobi to 15 DU for Yarmouth. The bias between the datasets ranges from -6.2 DU for Irene to 2.9 DU for Hohenpeissenberg. The mean bias between OMPS-LNM and ozonesondes is found to be -1.7±2.8 DU. Seven out of 22 sites exhibit a positive bias. Eleven sites show a bias within ±2 DU.

Site name (No. days)	Lat.	Lon.	~~sonde sonde OMPS-LNM~~ Ozonesonde mean~~std.~~ ±1σ ~~DU DU~~ [DU]	OMPS-LNM mean±1σ ~~DU~~ [DU]	Mean diff. ~~std.~~ mean±1σ ~~DU~~ [DU]	~~(Ozoneson~~
Legionowo (57)	52.4°N	21.0°E	37.4±7.4	35.1±9.2	-2.4±10.4	
Uccle (~~143~~138)	50.8°N	4.3°E	~~36.3~~36.4±7.2	34.3±9.9	~~-2.0~~-2.1±~~10.5~~10.4	
Hohenpeißenberg (132)	47.8°N	11.0°E	31.4±6.5	34.3±10.0	2.9±9.3	
Payerne (161)	46.8°N	6.9°E	34.8±7.3	36.8±10.4	2.0±11.1	
Yarmouth (~~67~~60)	43.9°N	66.1°W	~~36.8 8.0~~36.7±8.2	~~35.8~~35.5±15.5	~~15.4~~-1.3±15.3	
Sapporo (61)	43.1°N	141.3°E	39.6±9.9	34.0±15.3	-5.7±13.2	
Madrid (102)	40.5°N	3.7°W	~~35.4~~35.3±7.3	34.5±8.6	-0.8±8.6	
Boulder (61)	40.0°N	105.2°W	30.4±5.2	29.7±7.7	-0.7±7.3	
Wallops Island (88)	37.9°N	75.5°W	~~39.6~~39.5±8.5	41.1±12.0	1.5±10.5	
Tateno (85)	36.1°N	140.1°E	39.9±10.0	34.6±14.2	-5.3±11.9	
Naha (99)	26.2°N	127.7°E	39.1±9.6	36.8±11.5	-2.3±12.3	
Hilo (140)	19.4°N	155.4°W	33.5±10.5	30.0±10.1	-3.5±8.6	
Alajuela (63)	10.0°N	84.2°W	25.0±6.6	26.4±8.5	1.4±8.8	
Paramaribo (68)	5.8°N	55.2°W	29.7±6.3	24.3±8.8	-5.3±8.6	
Nairobi (98)	1.3°S	36.8°E	28.4±5.4	28.6±6.4	0.2±6.4	
Natal (72)	5.4°S	35.4°W	35.9~~8.2~~±8.1	30.8±7.9	-5.1±9.2	
Samoa (72)	14.4°S	170.6°W	21.6±5.1	~~23.4~~23.3±9.2	1.7±8.5	
La Réunion Island (117)	21.2°S	55.5°E	39.2~~8.6~~±8.5	34.4±8.6	-4.8±8.2	
Irene (65)	25.9°S	28.2°E	37.8±7.4	31.6±6.8	-6.2±8.9	
Broadmeadows (~~120~~121)	37.7°S	144.9°E	~~28.0~~28.1±6.3	~~26.0 7.9~~26.1±8.0	~~-1.9~~-2.0±8.3	
Lauder (110)	45.0°S	169.7°E	~~22.48~~22.5±3.8	20.0~~10.4~~±10.5	-2.4±10.4	
Macquarie Island (~~57~~58)	54.5°S	158.9°E	~~19.8 4.1~~19.5±4.4	~~21.6~~21.9±11.4	~~10.7~~2.3±11.9	

5.4 Comparison with OMI/MLS TOR and TROPOMI CCD datasets

The OMI/MLS TOR product is a tropospheric ozone dataset retrieved using the TOR technique with TOC from OMI and SOC from MLS profiles observed since 2004 (Ziemke et al., 2006). Both instruments are aboard the Aura satellite. Measurements of MLS are taken approximately 7 minutes before OMI. The OMI/MLS TOR product is available as monthly mean values on a $1° \times 1.25°$ (latitude/longitude) grid at https://acd-ext.gsfc.nasa.gov/Data_services/cloud_slice/new_data.html. The monthly means are obtained by subtracting daily means of SOC from TOC daily means and subsequent averaging. The TPH needed to determine SOC was obtained using the thermal definition of the tropopause from the NCEP re-analysis. A moving 2D (latitude/longitude) Gaussian function was used to fill gaps in SOC in the along-track direction, followed by a linear interpolation along the longitude. Daily global gridded maps were generated with $1° \times 1.25°$ spatial sampling. OMI TOMS L3 TOC data was filtered for clear-sky conditions by keeping only measurements with reflectivity less than 0.3. A comparison of OMI/MLS TOR with ozonesondes from September 2004 to August 2005 showed a difference of around 2 DU, with OMI/MLS being higher than the ozonesondes (Ziemke et al., 2006). For the comparison here, the OMPS-LNM data was re-gridded onto the OMI/MLS grid (1° lat × 1.25° lon) and averaged monthly.

The operational TrOC product from TROPOMI aboard S5P is derived with the CCD technique using the OFFL GODFIT V4 TOC (Hubert et al., 2021). The reference region, i.e. the region to estimate the above deep convective clouds column (ACCO), is the tropical eastern Indian and western Pacific oceans, 20°S-20°N and 70°E-170°W. The deep convective clouds are selected using a cloud fraction larger than 0.8, cloud albedo higher than 0.8, and effective cloud pressure less than 300 hPa. The ozone profile climatology of McPeters and Labow (2012) is used to estimate the ozone column from the retrieved cloud top pressure to the reference level of 270 hPa. The final adjusted ACCO values are averaged over five days and 0.5° latitude bins and smoothed using a running mean over 2.5° latitude. The TOC from cloud-free pixels with cloud fraction less than 0.1 are averaged over 3-days and binned into a $0.5° \times 1°$ (latitude/longitude) grid. The ACCO is subtracted from TOC for each grid cell. The final TrOC from the ground to the 270 hPa level is sampled daily and represents a clear-sky three-day running average (Hubert et al., 2021). Results of the validation of TROPOMI CCD by daily comparisons with SHADOZ ozonesondes from May 2018 to November 2021 are available online at http://mpc-vdaf-server.tropomi.eu/o3-tcl/o3-tcl-offl-ozone-sonde. A positive bias was found for nine SHADOZ sites, with a mean bias of 3.2 DU and a standard deviation of 1.8 DU.

In order to compare OMPS-LNM with TROPOMI CCD data, the vertical coverage of the latter dataset was extended from the 270 hPa pressure level to TPH ~~by~~ using the IUP-2018 ozone profile climatology. Furthermore, TROPOMI CCD data was ~~re-grided~~ re-gridded to the finer OMPS-LNM grid~~and~~, considering only OMPS-LNM grid cells with data, and then averaged monthly.

Figure 9 shows the mean difference between OMPS-LNM and TROPOMI CCD from May to December 2018 (top) and between OMPS-LNM and OMI/MLS from 2012 to 2018 (bottom). In general, the differences are negative. The overall bias is -1.8 ± 4.2 DU between OMPS-LNM and TROPOMI CCD, and -3.4 ± 4.7 DU between OMPS-LNM and OMI/MLS. This is consistent with the earlier validation results for TROPOMI CCD and OMI/MLS, which were found to be on average higher than ozonesonde data.
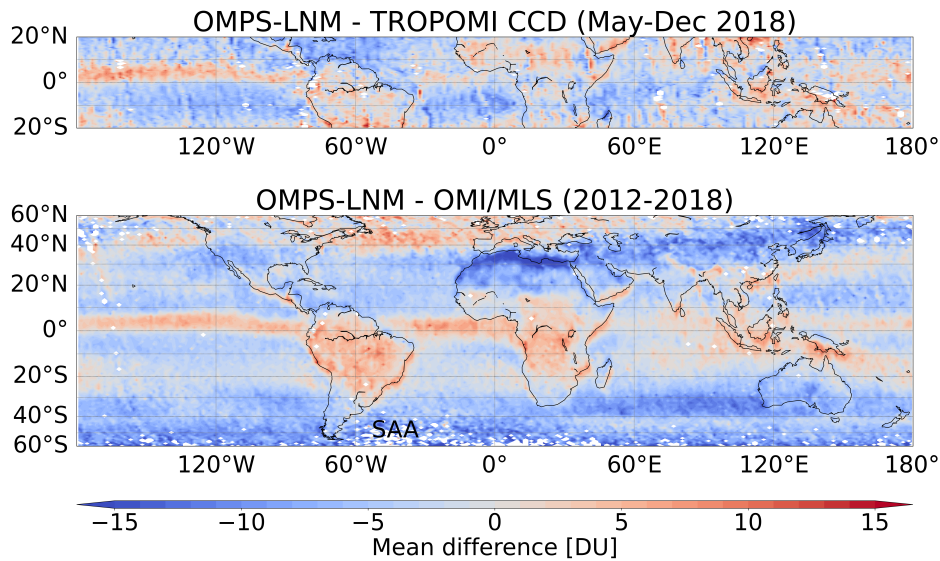
Figure 9. Mean differences in TrOC. Top panel: OMPS-LNM minus TROPOMI CCD from May to December 2018. Bottom panel: OMPS-LNM minus OMI/MLS from 2012 to 2018.

Both comparisons show similar patterns. Positive biases are observed ~~over~~ in South America, Middle Africa, and the Indonesian region. Over the oceans, the differences are mostly negative, between 0 and 10 DU. As discussed above, the band of positive bias is observed between 0° and 10°N over the Pacific and Atlantic oceans. The bias over the Pacific Ocean ranges from 5 to 10 DU, while over the Atlantic, it is below 5 DU. In ~~the~~ comparison with OMI/MLS, larger negative differences are observed in the southern extratropics that might result from the differences in the TPH definition. Over the northern extratropics, OMI/MLS shows higher values over Asia and North Africa, while OMPS-LNM is higher over the Atlantic Ocean. Higher values for OMPS-LNM are also observed in South America, Africa, and the Indonesian region. No seasonal variation in the differences is observed (not shown here). The general patterns observed in this comparison are similar to those seen in comparing the SOC from OMPS-LP and MLS (Fig. 7), indicating that the differences in TrOC are more influenced by the SOC.

Figure 10 shows monthly mean time series of TrOC (left panels) from OMPS-LNM (black), OMI/MLS (blue) and TROPOMI CCD (salmon) for six different zonal bands and differences between the OMPS-LNM and other datasets (right panels) from 2012 to 2018. Zonal bands from top to bottom are 40°N-60°N, 20°N-40°N, 0°-20°N, 0°-20°S, 20°S-40°S, and 40S°-60°S. Shadings mark the standard deviations of the averages and of the differences. In general, OMPS-LNM is lower than the other data, and the standard deviation of OMPS-LNM is higher than that of OMI/MLS. Very good agreement in the seasonal variation is observed, especially for the northern extratropics. In this latitude range, the mean difference between the OMPS-LNM and OMI/MLS is -2.0±3.2 DU for the 40°N-60°N band and -4.3±2 DU for 20°N-40°N. OMPS-LNM shows a negative trend in these zonal bands, which is more clearly observed in the difference panels. In the tropics, between the Equator and 20°N, no clear seasonality is observed for OMI/MLS. OMPS-LNM shows lower values during boreal winter, particularly low in 2015,

2016 and 2018. The TROPOMI CCD does not agree with the other two datasets in the northern tropical band. The mean bias of OMPS-LNM in this band is -1.6±2.6 DU with respect to OMI/MLS and -2.4±2.5 DU with respect to TROPOMI CCD. From 20°S to the Equator, OMI/MLS and OMPS-LNM agree with zero bias on average but show a difference of up to 5 DU in 2015 and 2016. In this region, the seasonal variability of TROPOMI CCD agrees with the other two datasets but shows a bias of -3.9±3.8 DU with respect to OMPS-LNM. From 20°S to 40°S, the seasonality of OMI/MLS data is similar to that of OMPS-LNM, and the mean bias between the datasets is -4.4±1.7 DU. In the 40S°-60°S band, the mean difference between the datasets reaches -7.6±3.9 DU. OMI/MLS shows a much weaker seasonality in this band. In contrast, OMPS-LNM shows more pronounced minima during austral autumn and maxima during austral spring.

6 Summary and conclusions

This study presents a scientific tropospheric ozone column (TrOC) dataset from Suomi NPP OMPS-NM/OMPS-LP observations employing the limb-nadir-matching (LNM) technique from 2012 to 2018. The data used in the retrieval, the retrieval approach, and the validation results of the OMPS-LNM TrOC dataset are discussed. A detailed analysis of the uncertainties of the underlying primary data, total ozone column (TOC), tropopause height (TPH) and stratospheric ozone column (SOC) is performed, and the overall uncertainty of the final TrOC product is estimated. Systematic and random components of the uncertainty are reported. The overall systematic TrOC uncertainty is estimated to be about 6.5 DU, and the overall random uncertainty is 12 DU for a single observation.

The OMPS-LNM TrOC data was validated using ozonesonde measurements and two TrOC satellite datasets, TROPOMI CCD (Hubert et al., 2021) and OMI/MLS TOR (Ziemke et al., 2006). The comparison with measurements from 22 ozonesondes sites shows a mean bias of -1.7 ± 2.8 DU with an average standard deviation of 9.9 DU. Half of the analysed sites show biases within 2 DU. We find a consistently negative bias when comparing OMPS-LNM TrOC with the two other satellite datasets. The mean bias between OMPS-LNM and OMI/MLS is -3.4 ± 4.7 DU, with ~~no seasonality in the differences~~ seasonal differences of up to 10 DU in the extratropics. Nevertheless, a good agreement in the long-term variability is observed. The mean bias between OMPS-LNM and TROPOMI CCD is -1.8 ± 4.2 DU.

A retrieval artefact is identified over the Pacific and Atlantic oceans, showing a band of TrOC values increased by about 10 DU between the Equator and 10°N. The source for this anomaly is believed to be the impact of the gradient in the reflectivity along the instrument Line-of-Sight (LOS) on the retrieval of ozone profiles from limb-scatter measurements (OMPS-LP). The reflectivity gradient is related to a persistent belt of high clouds in the ITCZ region.

The OMPS-LNM TrOC dataset is considered to be suitable for analysing the spatial and temporal variability of tropospheric ozone and evaluating atmospheric models. It is important to consider the ITCZ's effect on the retrieval results and that the global OMPS-LNM data are, on average, 1 to 4 DU lower than other datasets considered here. This bias is, however, well within the estimated systematic uncertainty of OMPS-LNM TrOC. A new version of IUP OMPS-LP profiles is being processed based on the improved L1 (V2.6) data that counts for the observed drift after 2018. Using the improved stratospheric data, the OMPS-LNM TrOC dataset will be reprocessed, extended to the present and will be subject of a later paper.
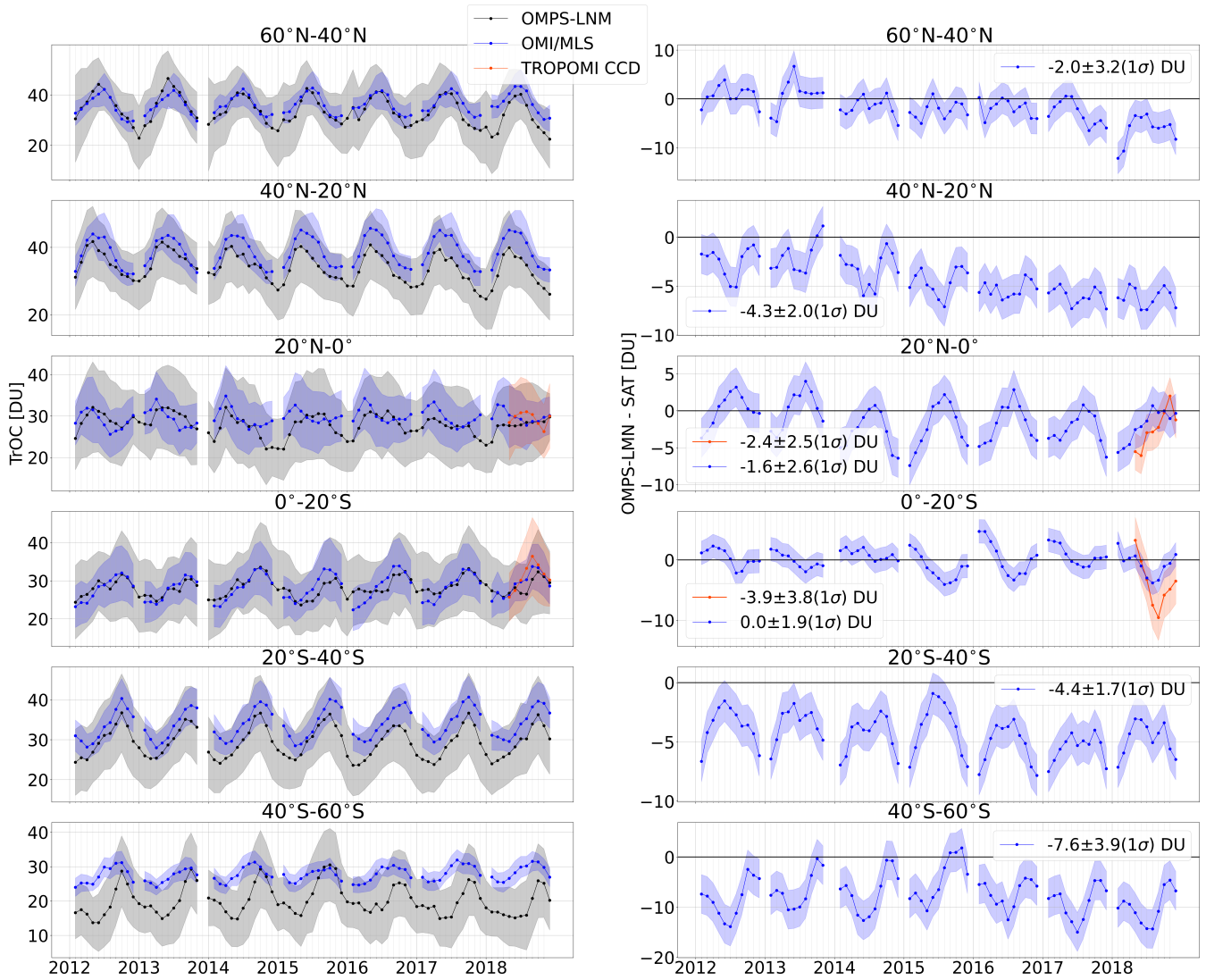
Figure 10. Zonal mean time series of TrOC from OMPS-LNM, OMI/MLS TOR and TROPOMI CCD (left) and differences between the OMPS-LNM and other datasets (right) for six zonal bands. The shadings indicate the standard deviations of TrOC and of the differences.

495 **Appendix A: Uncertainties in percentage**

Table A1. Final uncertainties values in percentage for three typical TrOC values.

TrOC case	Single measurement uncertainty		Total uncertainty of a L3 data point
[DU]	Systematic [%]	Random [%]	[%]
20	33	60	36
30	22	40	24
40	16	30	18

Author contributions. All authors contributed to the design of the study. AOC developed the retrieval algorithm, performed most of the computer calculations, and made the comparisons supervised by MW, AR, and ALW. JPB provided scientific conceptual input and oversight. CA wrote and performed the calculations of section 4.2. AOC led the preparation of the paper. All authors contributed to the paper's writing and editing.

References

Archibald, A. T., Neu, J. L., Elshorbany, Y. F., Cooper, O. R., Young, P. J., Akiyoshi, H., Cox, R. A., Coyle, M., Derwent, R. G., Deushi, M., Finco, A., Frost, G. J., Galbally, I. E., Gerosa, G., Granier, C., Griffiths, P. T., Hossaini, R., Hu, L., Jöckel, P., Josse, B., Lin, M. Y., Mertens, M., Morgenstern, O., Naja, M., Naik, V., Oltmans, S., Plummer, D. A., Revell, L. E., Saiz-Lopez, A., Saxena, P., Shin, Y. M., Shahid, I., Shallcross, D., Tilmes, S., Trickl, T., Wallington, T. J., Wang, T., Worden, H. M., and Zeng, G.: Tropospheric ozone assessment report: A critical review of changes in the tropospheric ozone burden and budget from 1850 to 2100, Elementa, 8, 1–53, https://doi.org/10.1525/elementa.2020.034, 2020.

Arosio, C.: Retrieval of ozone profiles from OMPS-LP observations and merging with SCIAMACHY and SAGE II time series to study long-term changes, Ph.D. thesis, Universität Bremen, 2019.

Arosio, C., Rozanov, A., Malinina, E., Eichmann, K.-U., Von Clarmann, T., and Burrows, J. P.: Retrieval of ozone profiles from OMPS limb scattering observations, Atmospheric Measurement Techniques, 11, 2135–2149, https://doi.org/10.5194/amt-11-2135-2018, 2018.

Arosio, C., Rozanov, A., Gorshelev, V., Laeng, A., and Burrows, J. P.: Assessment of the error budget for stratospheric ozone profiles retrieved from OMPS limb scatter measurements, Atmospheric Measurement Techniques, 15, 5949–5967, https://doi.org/10.5194/amt-15-5949-2022, 2022.

Boynard, A., Clerbaux, C., Coheur, P.-F., Hurtmans, D., Turquety, S., George, M., Hadji-Lazaro, J., Keim, C., and Meyer-Arnek, J.: Measurements of total and tropospheric ozone from IASI: comparison with correlative satellite, ground-based and ozonesonde observations, Atmospheric Chemistry and Physics, 9, 6255–6271, https://doi.org/10.5194/acp-9-6255-2009, 2009.

Coldewey-Egbers, M., Weber, M., Lamsal, L. N., de Beek, R., Buchwitz, M., and Burrows, J. P.: Total ozone retrieval from GOME UV spectral data using the weighting function DOAS approach, Atmospheric Chemistry and Physics, 5, 1015–1025, https://doi.org/10.5194/acp-5-1015-2005, 2005.

Cooper, O. R., Eckhardt, S., Crawford, J. H., Brown, C. C., Cohen, R. C., Bertram, T. H., Wooldridge, P., Perring, A., Brune, W. H., Ren, X., Brunner, D., and Baughcum, S. L.: Summertime buildup and decay of lightning NO x and aged thunderstorm outflow above North America, Journal of Geophysical Research: Atmospheres, 114, 1–18, https://doi.org/10.1029/2008JD010293, 2009.

Cuevas, E., González, Y., Rodríguez, S., Guerra, J. C., Gómez-Peláez, A. J., Alonso-Pérez, S., Bustos, J., and Milford, C.: Assessment of atmospheric processes driving ozone variations in the subtropical North Atlantic free troposphere, Atmospheric Chemistry and Physics, 13, 1973–1998, https://doi.org/10.5194/acp-13-1973-2013, 2013.

Daskalakis, N., Gallardo, L., Kanakidou, M., Nüß, J. R., Menares, C., Rondanelli, R., Thompson, A. M., and Vrekoussis, M.: Impact of biomass burning and stratospheric intrusions in the remote South Pacific Ocean troposphere, Atmospheric Chemistry and Physics, 22, 4075–4099, https://doi.org/10.5194/acp-22-4075-2022, 2022.

Doche, C., Dufour, G., Foret, G., Eremenko, M., Cuesta, J., Beekmann, M., and Kalabokas, P.: Summertime tropospheric-ozone variability over the Mediterranean basin observed with IASI, Atmospheric Chemistry and Physics, 14, 10 589–10 600, https://doi.org/10.5194/acp-14-10589-2014, 2014.

Ebojie, F., von Savigny, C., Ladstätter-Weißenmayer, A., Rozanov, A., Weber, M., Eichmann, K.-U., Bötel, S., Rahpoe, N., Bovensmann, H., and Burrows, J. P.: Tropospheric column amount of ozone retrieved from SCIAMACHY limb–nadir-matching observations, Atmospheric Measurement Techniques, 7, 2073–2096, https://doi.org/10.5194/amt-7-2073-2014, 2014.

Eichmann, K.-U., Lelli, L., von Savigny, C., Sembhi, H., and Burrows, J. P.: Global cloud top height retrieval using SCIAMACHY limb spectra: model studies and first results, Atmospheric Measurement Techniques, 9, 793–815, https://doi.org/10.5194/amt-9-793-2016, 2016.

Fioletov, V. E., Kerr, J. B., Hare, E. W., Labow, G. J., and McPeters, R. D.: An assessment of the world ground-based total ozone network performance from the comparison with satellite data, Journal of Geophysical Research: Atmospheres, 104, 1737–1747, https://doi.org/10.1029/1998JD100046, 1999.

Fishman, J. and Balok, A. E.: Calculation of daily tropospheric ozone residuals using TOMS and empirically improved SBUV measurements: Application to an ozone pollution episode over the eastern United States, Journal of Geophysical Research: Atmospheres, 104, 30 319–30 340, https://doi.org/10.1029/1999JD900875, 1999.

Fishman, J. and Larsen, J. C.: Distribution of total ozone and stratospheric ozone in the tropics: Implications for the distribution of tropospheric ozone, Journal of Geophysical Research, 92, 6627, https://doi.org/10.1029/JD092iD06p06627, 1987.

Fishman, J., Fakhruzzaman, K., Cros, B., and Nganga, D.: Identification of Widespread Pollution in the Southern Hemisphere Deduced from Satellite Analyses, Science, 252, 1693–1696, https://doi.org/10.1126/science.252.5013.1693, 1991.

Fishman, J., Wozniak, A. E., and Creilson, J. K.: Global distribution of tropospheric ozone from satellite measurements using the empirically corrected tropospheric ozone residual technique: Identification of the regional aspects of air pollution, Atmospheric Chemistry and Physics, 3, 893–907, https://doi.org/10.5194/acp-3-893-2003, 2003.

Flynn, L., Hornstein, J., and Hilsenrath, E.: The ozone mapping and profiler suite (OMPS), in: IEEE International IEEE International IEEE International Geoscience and Remote Sensing Symposium, 2004. IGARSS '04. Proceedings. 2004, vol. 1, pp. 152–155, IEEE, https://doi.org/10.1109/IGARSS.2004.1368968, 2004.

Flynn, L., Long, C., Wu, X., Evans, R., Beck, C. T., Petropavlovskikh, I., McConville, G., Yu, W., Zhang, Z., Niu, J., Beach, E., Hao, Y., Pan, C., Sen, B., Novicki, M., Zhou, S., and Seftor, C.: Performance of the Ozone Mapping and Profiler Suite (OMPS) products, Journal of Geophysical Research: Atmospheres, 119, 6181–6195, https://doi.org/10.1002/2013JD020467, 2014.

Garane, K., Koukouli, M.-E., Verhoelst, T., Lerot, C., Heue, K.-P., Fioletov, V., Balis, D., Bais, A., Bazureau, A., Dehn, A., Goutail, F., Granville, J., Griffin, D., Hubert, D., Keppens, A., Lambert, J.-C., Loyola, D., McLinden, C., Pazmino, A., Pommereau, J.-P., Redondas, A., Romahn, F., Valks, P., Van Roozendael, M., Xu, J., Zehner, C., Zerefos, C., and Zimmer, W.: TROPOMI/S5P total ozone column data: global ground-based validation and consistency with other satellite missions, Atmospheric Measurement Techniques, 12, 5263–5287, https://doi.org/10.5194/amt-12-5263-2019, 2019.

Gaudel, A., Cooper, O. R., Ancellet, G., Barret, B., Boynard, A., Burrows, J. P., Clerbaux, C., Coheur, P.-F., Cuesta, J., Cuevas, E., Doniki, S., Dufour, G., Ebojie, F., Foret, G., Garcia, O., Granados-Muñoz, M. J., Hannigan, J. W., Hase, F., Hassler, B., Huang, G., Hurtmans, D., Jaffe, D., Jones, N., Kalabokas, P., Kerridge, B., Kulawik, S., Latter, B., Leblanc, T., Le Flochmoën, E., Lin, W., Liu, J., Liu, X., Mahieu, E., McClure-Begley, A., Neu, J. L., Osman, M., Palm, M., Petetin, H., Petropavlovskikh, I., Querel, R., Rahpoe, N., Rozanov, A., Schultz, M. G., Schwab, J., Siddans, R., Smale, D., Steinbacher, M., Tanimoto, H., Tarasick, D. W., Thouret, V., Thompson, A. M., Trickl, T., Weatherhead, E., Wespes, C., Worden, H. M., Vigouroux, C., Xu, X., Zeng, G., and Ziemke, J.: Tropospheric Ozone Assessment Report: Present-day distribution and trends of tropospheric ozone relevant to climate and global atmospheric chemistry model evaluation, Elementa: Science of the Anthropocene, 6, https://doi.org/10.1525/elementa.291, 2018.

Goldberg, M. and Zhou, L.: The joint polar satellite system — Overview, instruments, proving ground and risk reduction activities, in: 2017 IEEE International Geoscience and Remote Sensing Symposium (IGARSS), vol. 2017-July, pp. 2776–2778, IEEE, https://doi.org/10.1109/IGARSS.2017.8127573, 2017.

Hersbach, H., Bell, B., Berrisford, P., Hirahara, S., Horányi, A., Muñoz-Sabater, J., Nicolas, J., Peubey, C., Radu, R., Schepers, D., Simmons, A., Soci, C., Abdalla, S., Abellan, X., Balsamo, G., Bechtold, P., Biavati, G., Bidlot, J., Bonavita, M., Chiara, G., Dahlgren, P., Dee, D., Diamantakis, M., Dragani, R., Flemming, J., Forbes, R., Fuentes, M., Geer, A., Haimberger, L., Healy, S., Hogan, R. J., Hólm, E.,

Janisková, M., Keeley, S., Laloyaux, P., Lopez, P., Lupu, C., Radnoti, G., Rosnay, P., Rozum, I., Vamborg, F., Villaume, S., and Thépaut, J.: The ERA5 global reanalysis, Quarterly Journal of the Royal Meteorological Society, 146, 1999–2049, https://doi.org/10.1002/qj.3803, 2020.

Heue, K.-P., Coldewey-Egbers, M., Delcloo, A., Lerot, C., Loyola, D., Valks, P., and van Roozendael, M.: Trends of tropical tropospheric 590 ozone from 20 years of European satellite measurements and perspectives for the Sentinel-5 Precursor, Atmospheric Measurement Techniques, 9, 5037–5051, https://doi.org/10.5194/amt-9-5037-2016, 2016.

Heue, K.-P., Eichmann, K.-U., and Valks, P.: TROPOMI/S5P ATBD of tropospheric ozone data products, https://sentinels.copernicus.eu/documents/247904/2476257/Sentinel-5P-ATBD-TROPOMI-Tropospheric-Ozone.pdf/d2106102-b5c3-4d28-b752-026e3448aab2?t=1625507455328, 2021.

595 Hoinka, K. P.: Statistics of the Global Tropopause Pressure, Monthly Weather Review, 126, 3303–3325, https://doi.org/10.1175/1520-0493(1998)126<3303:SOTGTP>2.0.CO;2, 1998.

Hubert, D., Heue, K.-P., Lambert, J.-C., Verhoelst, T., Allaart, M., Compernolle, S., Cullis, P. D., Dehn, A., Félix, C., Johnson, B. J., Keppens, A., Kollonige, D. E., Lerot, C., Loyola, D., Maata, M., Mitro, S., Mohamad, M., Piters, A., Romahn, F., Selkirk, H. B., da Silva, F. R., Stauffer, R. M., Thompson, A. M., Veefkind, J. P., Vömel, H., Witte, J. C., and Zehner, C.: TROPOMI tropospheric ozone column data: 600 geophysical assessment and comparison to ozonesondes, GOME-2B and OMI, Atmospheric Measurement Techniques, 14, 7405–7433, https://doi.org/10.5194/amt-14-7405-2021, 2021.

Jaross, G.: OMPS-NPP L2 NM Ozone (O3) Total Column swath orbital V2, Greenbelt, MD, USA, Goddard Earth Sciences Data and Information Services Center (GES DISC), Accessed: [18 July 2023], https://doi.org/10.5067/0WF4HAAZ0VHK, 2017.

Jenkins, G. S. and Ryu, J.-H.: Space-borne observations link the tropical atlantic ozone maximum and paradox to lightning, Atmospheric 605 Chemistry and Physics, 4, 361–375, https://doi.org/10.5194/acp-4-361-2004, 2004.

Jia, J.: Improvement and interpretation of the tropospheric ozone columns retrieved based on SCIAMACHY Limb-Nadir Matching approach, Ph.D. thesis, Universität Bremen, http://nbn-resolving.de/urn:nbn:de:gbv:46-00105374-15, 2016.

Jia, J., Rozanov, A., Ladstätter-Weißenmayer, A., and Burrows, J. P.: Global validation of SCIAMACHY limb ozone data (versions 2.9 and 3.0, IUP Bremen) using ozonesonde measurements, Atmospheric Measurement Techniques, 8, 3369–3383, https://doi.org/10.5194/amt-610 8-3369-2015, 2015.

Jia, J., Ladstätter-Weißenmayer, A., Hou, X., Rozanov, A., and Burrows, J. P.: Tropospheric ozone maxima observed over the Arabian Sea during the pre-monsoon, Atmospheric Chemistry and Physics, 17, 4915–4930, https://doi.org/10.5194/acp-17-4915-2017, 2017.

Kourtidis, K.: Regional levels of ozone in the troposphere over eastern Mediterranean, Journal of Geophysical Research, 107, 8140, https://doi.org/10.1029/2000JD000140, 2002.

615 Kramarova, N. A., Bhartia, P. K., Jaross, G., Moy, L., Xu, P., Chen, Z., DeLand, M., Froidevaux, L., Livesey, N., Degenstein, D., Bourassa, A., Walker, K. A., and Sheese, P.: Validation of ozone profile retrievals derived from the OMPS LP version 2.5 algorithm against correlative satellite measurements, Atmospheric Measurement Techniques, 11, 2837–2861, https://doi.org/10.5194/amt-11-2837-2018, 2018.

Ladstätter-Weißenmayer, A., Meyer-Arnek, J., Schlemm, A., and Burrows, J. P.: Influence of stratospheric airmasses on tropospheric vertical O3 columns based on GOME (Global Ozone Monitoring Experiment) measurements and backtrajectory calculation over the Pacific, 620 Atmospheric Chemistry and Physics, 4, 903–909, https://doi.org/10.5194/acp-4-903-2004, 2004.

Leventidou, E., Eichmann, K.-U., Weber, M., and Burrows, J. P.: Tropical tropospheric ozone columns from nadir retrievals of GOME-1/ERS-2, SCIAMACHY/Envisat, and GOME-2/MetOp-A (1996–2012), Atmospheric Measurement Techniques, 9, 3407–3427, https://doi.org/10.5194/amt-9-3407-2016, 2016.

Leventidou, E., Weber, M., Eichmann, K.-U., Burrows, J. P., Heue, K. P., Thompson, A. M., and Johnson, B. J.: Harmonisation and trends of 20-year tropical tropospheric ozone data, Atmospheric Chemistry and Physics, 18, 9189–9205, https://doi.org/10.5194/acp-18-9189-2018, 2018.

Liu, H., Chang, W. L., Oltmans, S. J., Chan, L. Y., and Harris, J. M.: On springtime high ozone events in the lower troposphere from Southeast Asian biomass burning, Atmospheric Environment, 33, 2403–2410, https://doi.org/10.1016/S1352-2310(98)00357-4, 1999.

Liu, J., Rodriguez, J. M., Steenrod, S. D., Douglass, A. R., Logan, J. A., Olsen, M. A., Wargan, K., and Ziemke, J. R.: Causes of inter-annual variability over the southern hemispheric tropospheric ozone maximum, Atmospheric Chemistry and Physics, 17, 3279–3299, https://doi.org/10.5194/acp-17-3279-2017, 2017.

Logan, J. A.: Tropospheric ozone: seasonal behavior, trends, and anthropogenic influence., Journal of Geophysical Research, 90, 10 463–10 482, https://doi.org/10.1029/JD090iD06p10463, 1985.

Malicet, J., Daumont, D., Charbonnier, J., Parisse, C., Chakir, A., and Brion, J.: Ozone UV spectroscopy. II. Absorption cross-sections and temperature dependence, Journal of Atmospheric Chemistry, 21, 263–273, https://doi.org/10.1007/BF00696758, 1995.

McPeters, R., Frith, S., Kramarova, N., Ziemke, J., and Labow, G.: Trend quality ozone from NPP OMPS: the version 2 processing, Atmospheric Measurement Techniques, 12, 977–985, https://doi.org/10.5194/amt-12-977-2019, 2019.

McPeters, R. D. and Labow, G. J.: Climatology 2011: An MLS and sonde derived ozone climatology for satellite retrieval algorithms, Journal of Geophysical Research: Atmospheres, 117, n/a–n/a, https://doi.org/10.1029/2011JD017006, 2012.

McPeters, R. D., Frith, S., and Labow, G. J.: OMI total column ozone: extending the long-term data record, Atmospheric Measurement Techniques, 8, 4845–4850, https://doi.org/10.5194/amt-8-4845-2015, 2015.

Mettig, N., Weber, M., Rozanov, A., Burrows, J. P., Veefkind, P., Thompson, A. M., Stauffer, R. M., Leblanc, T., Ancellet, G., Newchurch, M. J., Kuang, S., Kivi, R., Tully, M. B., Van Malderen, R., Piters, A., Kois, B., Stübi, R., and Skrivankova, P.: Combined UV and IR ozone profile retrieval from TROPOMI and CrIS measurements, Atmospheric Measurement Techniques, 15, 2955–2978, https://doi.org/10.5194/amt-15-2955-2022, 2022.

Miles, G. M., Siddans, R., Kerridge, B. J., Latter, B. G., and Richards, N. A. D.: Tropospheric ozone and ozone profiles retrieved from GOME-2 and their validation, Atmospheric Measurement Techniques, 8, 385–398, https://doi.org/10.5194/amt-8-385-2015, 2015.

Monks, P. S., Archibald, A. T., Colette, A., Cooper, O., Coyle, M., Derwent, R., Fowler, D., Granier, C., Law, K. S., Mills, G. E., Stevenson, D. S., Tarasova, O., Thouret, V., von Schneidemesser, E., Sommariva, R., Wild, O., and Williams, M. L.: Tropospheric ozone and its precursors from the urban to the global scale from air quality to short-lived climate forcer, Atmospheric Chemistry and Physics, 15, 8889–8973, https://doi.org/10.5194/acp-15-8889-2015, 2015.

Ohyama, H., Kawakami, S., Shiomi, K., and Miyagawa, K.: Retrievals of Total and Tropospheric Ozone From GOSAT Thermal Infrared Spectral Radiances, IEEE Transactions on Geoscience and Remote Sensing, 50, 1770–1784, https://doi.org/10.1109/TGRS.2011.2170178, 2012.

Oltmans, S. J.: Tropospheric ozone over the North Pacific from ozonesonde observations, Journal of Geophysical Research, 109, D15S01, https://doi.org/10.1029/2003JD003466, 2004.

Orfanoz-Cheuquelaf, A., Rozanov, A., Weber, M., Arosio, C., Ladstätter-Weißenmayer, A., and Burrows, J. P.: Total ozone column from Ozone Mapping and Profiler Suite Nadir Mapper (OMPS-NM) measurements using the broadband weighting function fitting approach (WFFA), Atmospheric Measurement Techniques, 14, 5771–5789, https://doi.org/10.5194/amt-14-5771-2021, 2021.

Pavón-Carrasco, F. J. and De Santis, A.: The South Atlantic Anomaly: The Key for a Possible Geomagnetic Reversal, Frontiers in Earth Science, 4, 1–9, https://doi.org/10.3389/feart.2016.00040, 2016.

Rodgers, C. D.: Inverse methods for atmospheres: Theory and practice, vol. 2, 2000.

Rowland, F. S., Angell, J., Attmannspacher, W., Bloomfield, P., Bojkov, R., Harris, N., Komhyr, W., McFarland, M., McPeters, R., and Stolarski, R.: Trends in Total Column Ozone Measurements. In: Report of the Interantional ozone Trends Panel 1988, Tech. rep., World Meteorological Organization, https://doi.org/https://csl.noaa.gov/assessments/ozone/1988/report.html, 1988.

Sauvage, B., Martin, R. V., van Donkelaar, A., and Ziemke, J. R.: Quantification of the factors controlling tropical tropospheric ozone and the South Atlantic maximum, Journal of Geophysical Research, 112, D11 309, https://doi.org/10.1029/2006JD008008, 2007.

Schoeberl, M. R., Ziemke, J. R., Bojkov, B., Livesey, N., Duncan, B., Strahan, S., Froidevaux, L., Kulawik, S., Bhartia, P. K., Chandra, S., Levelt, P. F., Witte, J. C., Thompson, A. M., Cuevas, E., Redondas, A., Tarasick, D. W., Davies, J., Bodeker, G., Hansen, G., Johnson, B. J., Oltmans, S. J., Vömel, H., Allaart, M., Kelder, H., Newchurch, M., Godin-Beekmann, S., Ancellet, G., Claude, H., Andersen, S. B., Kyrö, E., Parrondos, M., Yela, M., Zablocki, G., Moore, D., Dier, H., von der Gathen, P., Viatte, P., Stübi, R., Calpini, B., Skrivankova, P., Dorokhov, V., de Backer, H., Schmidlin, F. J., Coetzee, G., Fujiwara, M., Thouret, V., Posny, F., Morris, G., Merrill, J., Leong, C. P., Koenig-Langlo, G., and Joseph, E.: A trajectory-based estimate of the tropospheric ozone column using the residual method, Journal of Geophysical Research, 112, D24S49, https://doi.org/10.1029/2007JD008773, 2007.

Schultz, M. G., Akimoto, H., Bottenheim, J., Buchmann, B., Galbally, I. E., Gilge, S., Helmig, D., Koide, H., Lewis, A. C., Novelli, P. C., Plass-Dölmer, C., Ryerson, T. B., Steinbacher, M., Steinbrecher, R., Tarasova, O., Tørseth, K., Thouret, V., and Zellweger, C.: The global atmosphere watch reactive gases measurement network, Elementa, 3, 1–23, https://doi.org/10.12952/journal.elementa.000067, 2015.

Seftor, C. and Johnson, J.: README Document for Suomi-NPP OMPS NMTO3-L2 Product, https://snpp-omps.gesdisc.eosdis.nasa.gov/data/SNPP_OMPS_Level2/OMPS_NPP_NMTO3_L2.2/doc/README.OMPS_NPP_NMTO3_L2.2.pdf, 2017.

Seftor, C. J., Jaross, G., Kowitt, M., Haken, M., Li, J., and Flynn, L. E.: Postlaunch performance of the Suomi National Polar-orbiting Partnership Ozone Mapping and Profiler Suite (OMPS) nadir sensors, Journal of Geophysical Research: Atmospheres, 119, 4413–4428, https://doi.org/10.1002/2013JD020472, 2014.

Serdyuchenko, A., Gorshelev, V., Weber, M., Chehade, W., and Burrows, J. P.: High spectral resolution ozone absorption cross-sections – Part 2: Temperature dependence, Atmospheric Measurement Techniques, 7, 625–636, https://doi.org/10.5194/amt-7-625-2014, 2014.

Shindell, D. T., Faluvegi, G., Lacis, A., Hansen, J., Ruedy, R., and Aguilar, E.: Role of tropospheric ozone increases in 20th-century climate change, Journal of Geophysical Research Atmospheres, 111, 1–11, https://doi.org/10.1029/2005JD006348, 2006.

Škerlak, B., Sprenger, M., and Wernli, H.: A global climatology of stratosphere–troposphere exchange using the ERA-Interim data set from 1979 to 2011, Atmospheric Chemistry and Physics, 14, 913–937, https://doi.org/10.5194/acp-14-913-2014, 2014.

Stevenson, D. S., Young, P. J., Naik, V., Lamarque, J.-F., Shindell, D. T., Voulgarakis, A., Skeie, R. B., Dalsoren, S. B., Myhre, G., Berntsen, T. K., Folberth, G. A., Rumbold, S. T., Collins, W. J., MacKenzie, I. A., Doherty, R. M., Zeng, G., van Noije, T. P. C., Strunk, A., Bergmann, D., Cameron-Smith, P., Plummer, D. A., Strode, S. A., Horowitz, L., Lee, Y. H., Szopa, S., Sudo, K., Nagashima, T., Josse, B., Cionni, I., Righi, M., Eyring, V., Conley, A., Bowman, K. W., Wild, O., and Archibald, A.: Tropospheric ozone changes, radiative forcing and attribution to emissions in the Atmospheric Chemistry and Climate Model Intercomparison Project (ACCMIP), Atmospheric Chemistry and Physics, 13, 3063–3085, https://doi.org/10.5194/acp-13-3063-2013, 2013.

Szopa, S., Naik, V., Adhikary, B., Artaxo, P., Berntsen, T., Collins, W. D., Fuzzi, S., Gallardo, L., Kiendler-Scharr, A., Klimont, Z., Liao, H., Unger, N., and Zanis, P.: 2021: Short-lived Climate Forcers, in: Climate Change 2021 – The Physical Science Basis. Contribution of Working Group I to the Sixth Assessment Report of the Intergovernmental Panel on Climate Change, edited by Masson-Delmotte, V., Zhai, P., Pirani, A., Connors, S., Péan, C., Berger, S., Caud, N., Chen, Y., Goldfarb, L., Gomis, M., Huang, M., Leitzell, K., Lonnoy,

E., Matthews, J., Maycock, T., Waterfield, T., Yelekci, O., Yu, R., and Zhou, B., pp. 817–922, Cambridge University Press, Cambridge, United Kingdom and New York, NY, US, https://doi.org/10.1017/9781009157896.008, 2023.

Thompson, A. M., Witte, J. C., Sterling, C., Jordan, A., Johnson, B. J., Oltmans, S. J., Fujiwara, M., Vömel, H., Allaart, M., Piters, A., Coetzee, G. J., Posny, F., Corrales, E., Diaz, J. A., Félix, C., Komala, N., Lai, N., Ahn Nguyen, H. T., Maata, M., Mani, F., Zainal, Z., Ogino, S. Y., Paredes, F., Penha, T. L. B., da Silva, F. R., Sallons-Mitro, S., Selkirk, H. B., Schmidlin, F. J., Stübi, R., and Thiongo, K.: First reprocessing of southern hemisphere additional ozonesondes (SHADOZ) ozone profiles (1998–2016): 2. comparisons with satellites and ground-based instruments, Journal of Geophysical Research: Atmospheres, 122, 13,000–13,025, https://doi.org/10.1002/2017JD027406, 2017.

Valks, P., Hao, N., Gimeno Garcia, S., Loyola, D., Dameris, M., Jöckel, P., and Delcloo, A.: Tropical tropospheric ozone column retrieval for GOME-2, Atmospheric Measurement Techniques, 7, 2513–2530, https://doi.org/10.5194/amt-7-2513-2014, 2014.

Weber, M., Arosio, C., Coldewey-Egbers, M., Fioletov, V. E., Frith, S. M., Wild, J. D., Tourpali, K., Burrows, J. P., and Loyola, D.: Global total ozone recovery trends attributed to ozone-depleting substance (ODS) changes derived from five merged ozone datasets, Atmospheric Chemistry and Physics, 22, 6843–6859, https://doi.org/10.5194/acp-22-6843-2022, 2022.

Witte, J. C., Thompson, A. M., Smit, H. G., Fujiwara, M., Posny, F., Coetzee, G. J., Northam, E. T., Johnson, B. J., Sterling, C. W., Mohamad, M., Ogino, S. Y., Jordan, A., and da Silva, F. R.: First reprocessing of Southern Hemisphere ADditional OZonesondes (SHADOZ) profile records (1998-2015): 1. Methodology and evaluation, Journal of Geophysical Research, 122, 6611–6636, https://doi.org/10.1002/2016JD026403, 2017.

WMO (World Meteorological Organization): Meteorology – A three-dimensional science: Second ses- sion ofthe commission for aerology, WMO Bull., VI, 1957.

Young, P. J., Archibald, A. T., Bowman, K. W., Lamarque, J.-F., Naik, V., Stevenson, D. S., Tilmes, S., Voulgarakis, A., Wild, O., Bergmann, D., Cameron-Smith, P., Cionni, I., Collins, W. J., Dalsøren, S. B., Doherty, R. M., Eyring, V., Faluvegi, G., Horowitz, L. W., Josse, B., Lee, Y. H., MacKenzie, I. A., Nagashima, T., Plummer, D. A., Righi, M., Rumbold, S. T., Skeie, R. B., Shindell, D. T., Strode, S. A., Sudo, K., Szopa, S., and Zeng, G.: Pre-industrial to end 21st century projections of tropospheric ozone from the Atmospheric Chemistry and Climate Model Intercomparison Project (ACCMIP), Atmospheric Chemistry and Physics, 13, 2063–2090, https://doi.org/10.5194/acp-13-2063-2013, 2013.

Zängl, G. and Hoinka, K. P.: The Tropopause in the Polar Regions, Journal of Climate, 14, 3117–3139, https://doi.org/10.1175/1520-0442(2001)014<3117:TTITPR>2.0.CO;2, 2001.

Ziemke, J. R.: Supplement of: Trends in global tropospheric ozone inferred from a composite record of TOMS/OMI/MLS/OMPS satellite measurements and the MERRA-2 GMI simulation, Supplement of Atmos. Chem. Phys, 19, 3257–3269, https://doi.org/10.5194/acp-19-3257-2019-supplement, 2019.

Ziemke, J. R., Chandra, S., and Bhartia, P. K.: Two new methods for deriving tropospheric column ozone from TOMS measurements: Assimilated UARS MLS/HALOE and convective-cloud differential techniques, Journal of Geophysical Research: Atmospheres, 103, 22 115–22 127, https://doi.org/10.1029/98JD01567, 1998.

Ziemke, J. R., Chandra, S., Duncan, B. N., Froidevaux, L., Bhartia, P. K., Levelt, P. F., and Waters, J. W.: Tropospheric ozone determined from Aura OMI and MLS: Evaluation of measurements and comparison with the Global Modeling Initiative's Chemical Transport Model, Journal of Geophysical Research, 111, D19 303, https://doi.org/10.1029/2006JD007089, 2006.

735   Ziemke, J. R., Chandra, S., Labow, G. J., Bhartia, P. K., Froidevaux, L., and Witte, J. C.: A global climatology of tropospheric and stratospheric ozone derived from Aura OMI and MLS measurements, Atmospheric Chemistry and Physics, 11, 9237–9251, https://doi.org/10.5194/acp-11-9237-2011, 2011.

Ziemke, J. R., Oman, L. D., Strode, S. A., Douglass, A. R., Olsen, M. A., McPeters, R. D., Bhartia, P. K., Froidevaux, L., Labow, G. J., Witte, J. C., Thompson, A. M., Haffner, D. P., Kramarova, N. A., Frith, S. M., Huang, L.-K., Jaross, G. R., Seftor, C. J., Deland, M. T., and Taylor,

740   S. L.: Trends in global tropospheric ozone inferred from a composite record of TOMS/OMI/MLS/OMPS satellite measurements and the MERRA-2 GMI simulation, Atmospheric Chemistry and Physics, 19, 3257–3269, https://doi.org/10.5194/acp-19-3257-2019, 2019.